

This is the peer reviewed version of the following article:

Evidence of subduction-related components in sapphirine-bearing gabbroic dykes (Finero phlogopite-peridotite): Insights into the source of the Triassic-Jurassic magmatism at the Europe-Africa boundary / Giovanardi, Tommaso; Zanetti, Alberto; Dallai, Luigi; Morishita, Tomoaki; Hémond, Christophe; Mazzucchelli, Maurizio. - In: LITHOS. - ISSN 0024-4937. - 354-355:(2020), pp. 1-16. [10.1016/j.lithos.2020.105366]

Terms of use:

The terms and conditions for the reuse of this version of the manuscript are specified in the publishing policy. For all terms of use and more information see the publisher's website.

13/03/2024 10:06

**Evidence of subduction-related components in sapphirine-bearing gabbroic dykes (Finero
Phlogopite–Peridotite): Insights into the source of the Triassic–Jurassic magmatism at the
Europe–Africa boundary**

Tommaso Giovanardi^{1,2#}, Alberto Zanetti^{3#}, Luigi Dallai⁴, Tomoaki Morishita⁵, Christophe
Hémond⁶, Maurizio Mazzucchelli^{2*}

¹DIPARTIMENTO DI SCIENZE DELLA TERRA E DELL'AMBIENTE, UNIVERSITA' DEGLI
STUDI DI PAVIA, VIA FERRATA 1, 27100 PAVIA, ITALY

²DIPARTIMENTO DI SCIENZE CHIMICHE E GEOLOGICHE, UNIVERSITA' DEGLI STUDI
DI MODENA E REGGIO EMILIA, VIA CAMPI 103, 41121 MODENA, ITALY

³ISTITUTO DI GEOSCIENZE E GEORISORSE-C.N.R. PAVIA, VIA FERRATA 1, 27100
PAVIA, ITALY

⁴ISTITUTO DI GEOSCIENZE E GEORISORSE-C.N.R. PISA, VIA MORUZZI 1, 56124 PISA,
ITALY

⁵FRONTIER SCIENCE ORGANIZATION, KANAZAWA UNIVERSITY, 920-1192
KANAZAWA, JAPAN

⁶LABORATOIRE GÉOSCIENCES OCÉAN, UMR6538, INSTITUT UNIVERSITAIRE
EUROPÉEN DE LA MER, UNIVERSITÉ DE BREST & CNRS, PLACE NICOLAS COPERNIC,
F-29280, PLOUZANÉ, FRANCE.

these authors are equal first authors of this work

* Corresponding author: maurizio.mazzucchelli@unimore.it

Keywords: sapphirine; Finero; mantle peridotite; dykes; Ivrea Verbano

27 **Abstract**

28 A gabbroic dyke swarm containing magmatic sapphirine occurs in the Finero phlogopite–peridotite
29 (FPP), one of the major mantle massifs in the Ivrea–Verbano Zone (IVZ; western Southern Alps).
30 Sapphirine is part of a particular mineral assemblage, including plagioclase, titanian pargasite,
31 titanian phlogopite, and Cl-rich apatite; the latter mineral hosts calcite inclusions. The dykes cut the
32 mantle foliation at a high angle, are bounded by orthopyroxenite layers, and show symmetric
33 internal banding, represented by two outer hornblendite selvages and an inner leucogabbro band.
34 The sapphirine occurs in up to 3 cm-thick irregular patches in both hornblendite selvages, along
35 with Al-rich amphibole and green spinel.

36 We present major and trace elements of minerals and bulk rock, as well as mineral O, Sr, and Nd
37 isotopic compositions of dykes and the host peridotite from two different outcrops in the FPP area.

38 Our data show that early melt migration developed through porous flow within cm-thick channels
39 and was characterised by orthopyroxene dissolution. Following progressive percolation and
40 reaction, the melt became silica saturated with segregation of orthopyroxenite in the centres of the
41 channels. The banded internal structure of the dykes was caused by three different evolutionary
42 stages, involving opening and enlargement of the conduits. The sapphirine and green spinel
43 segregation took place at $T > 1,000\text{ }^{\circ}\text{C}$, in the presence of melt with transient composition, which
44 interstitially migrated and reacted with the cumulus minerals to form the hornblendite layers. The
45 mineral chemistry of the newly-formed amphiboles indicates that the sapphirine parental melt was
46 Al-rich, depleted to strongly depleted in Hf, Zr, Nb, Ta, Ti, Sc, V, and middle and heavy rare earth
47 elements, and characterised by a positive Eu anomaly and $(\text{Zr/Hf})_{\text{N}} < 1$. These data suggest a
48 parental melt with a significant amount of normative plagioclase. However, the studied veins do not
49 show evidence of plagioclase assimilation, and we argue that this process could have occurred in
50 magmatic bodies that are not outcropping today to the surface or in the melt source.

51 The $\delta^{18}\text{O}$ values of vein amphiboles and plagioclases vary from 6.9 to 8.6‰ SMOW, which is well
52 above the mantle range, even when considering fractionation upon cooling. Given that

orthopyroxene from the wall has “normal” mantle $\delta^{18}\text{O}$ values (5.8‰), reaction with the host metasomatised peridotite cannot be responsible for the heavy $\delta^{18}\text{O}$ signature, and the latter must have been imparted by crustal components deeper in the mantle. Our petrographic and geochemical evidence demonstrates that the northern IVZ records an extremely prolonged release, from the Variscan orogenic cycle to the Mesozoic exhumation, of K- H_2O -rich mantle-derived melts, mixed with subduction-related components. This finding provides valuable insights into the Triassic–Jurassic magmatism and the geodynamic environment at the Europe–Africa boundary.

61

62 **1. Introduction**

It is well known that the subcontinental lithospheric mantle (SCLM) may record significant heterogeneities in terms of both lithology and geochemical composition, resulting from the development of different tectono-magmatic events over a long time span (Mukasa and Shervais, 1999; Rivalenti et al., 2007a, b; Mazzucchelli et al., 2009; 2010; 2016; Borghini et al., 2017; Princivale et al., 2014; Ponce et al., 2015; Rocco et al., 2017; Consuma et al., 2019). The petrochemical records of the lithospheric mantle and uprising melts can be very different based on the geochemical affinity of the melt, the composition of the peridotite mantle column, the modalities of melt migration, and the P , T , $f\text{O}_2$, and $f\text{H}_2$ conditions of the system. An exceptional locality where this can be studied in great detail is the phlogopite–peridotite mantle unit of Finero (Cawthorn, 1975; Siena & Coltorti, 1989). The Finero phlogopite–peridotite (FPP) is one of the most studied mantle massifs on Earth. It crops out in the northernmost part of the Ivrea–Verbano Zone (IVZ, western Southern Alps, Italy; Fig. 1) and consists of an association of phlogopite-bearing amphibole harzburgites and dunites, both locally associated with phlogopite-bearing amphibole pyroxenites. This is the result of an important episode of pervasive to channelled porous flow migration of melts containing a large volume of crustal components that induced virtually complete metasomatic recrystallisation of an older sequence of harzburgite and pyroxenite

79 associations (Lensch, 1968; Cawthorn, 1975; Griffin & O'Reilly, 1986; Siena & Coltorti, 1989;
 80 Shervais and Musaka, 1991; Hartmann & Wedepohl, 1993; Zanetti et al., 1999, 2016; Grieco et al.,
 81 2001, 2004; Morishita et al., 2003, 2008; Raffone et al., 2006; Selverstone & Sharp, 2011;
 82 Mazzucchelli et al., 2014; Tommasi et al., 2017). The crustal affinity of these metasomatic melts is
 83 implied by high $\delta^{18}\text{O}$ values and by the Nd, Sr, Pb, H, S, Cl, and noble gas isotopic compositions of
 84 the FPP rocks (Hunziker and Zingg, 1982; Voshage et al., 1987, 1988; Cumming et al., 1987;
 85 Hartmann and Wedepohl, 1993; Obermiller, 1994; Seitz and Woodland, 2000; Downes, 2001;
 86 Matsumoto et al., 2005; Selverstone and Sharp, 2011). The melt migration processes have been
 87 mainly attributed to supra-subduction environments (e.g. Zanetti et al., 1999; Grieco et al., 2001,
 88 2004; Morishita et al., 2003, 2008; Matsumoto et al., 2005), but also to extensional settings (Garuti
 89 et al., 2001; Zaccarini et al., 2004).

90 The available geochronological data indicate that this main event of melt migration took place in
 91 the Palaeozoic (Zanetti et al., 2016; Malitch et al., 2017), but many field, petrochemical, and
 92 geochronological data point to the development of several other tectono-magmatic events in the
 93 Mesozoic as well (Stähle et al., 1990, 2001; Grieco et al., 2001; Matsumoto et al., 2005; Morishita
 94 et al., 2003, 2008; Zanetti et al., 1999; 2016; Malitch et al., 2017).

95 Giovanardi et al. (2013) studied the occurrence of a late sapphirine-bearing gabbroic dykelet swarm
 96 previously reported by Siena & Coltorti (1989) and discovered by M. Mazzucchelli (Giovanardi et
 97 al., 2013). Based on a detailed petrographic and geochemical survey, they provided evidence for a
 98 multi-stage dyke formation, which involved fractional crystallisation associated with different
 99 patterns of melt–rock interactions.

100 With the aim of better constraining the nature of the primitive melt and petrological processes and
 101 inducing the segregation of sapphirine in the dykes, in this paper, new and detailed petrochemical
 102 data are reported for dykes and host peridotites close to the area studied by Giovanardi et al. (2013)
 103 and on a second finding in an adjacent area. Particular care has been dedicated to characterising the
 104 compositional variability in terms of major and trace element mineral chemistry, as well as the

105 mineral O, Nd, and Sr isotopic composition, to document the geochemical fractionation of the
106 flowing melt following reaction with the host peridotite and early cumulates. The genetic and
107 temporal relationships between the dyke emplacement and other events of melt migration recorded
108 by the FPP unit, as well as the related geodynamic scenarios, are also addressed.

109

110 **2. Geological setting**

111 In the Finero area (Fig. 1), the IVZ crops out in a pseudo-antiform structure with the FPP mantle
112 unit at the core, flanked by what has been called the Finero Mafic Complex (Cawthorn, 1975; Siena
113 & Coltorti, 1989; Lu et al., 1997a, b; Zanetti et al., 2013, 2014; Giovanardi et al., 2014;
114 Mazzucchelli et al., 2014; Langone et al., 2017). The Mafic Complex is divided into three different
115 units: the stratigraphically lower Layered Internal Zone unit (LIZ), in contact with the FPP; the
116 Amphibole-Peridotite (Amphibole-Pd); and the External Gabbro (EG). The EG is placed in tectonic
117 contact with the Amphibole-Peridotite by a Mesozoic high-T shear-zone (Langone et al., 2018). A
118 tectonic contact also characterises the transition toward the amphibolite-facies metasediments and
119 metabasites of the Kinzigite Formation (KF), which represent the metamorphic basement of the
120 Adria Plate. Septa of KF rocks are embedded in the EG.

121 The Finero mafic-ultramafic sequence presents several differences with respect to the southern and
122 central sectors of the IVZ (i.e. the Baldissero and Balmuccia peridotites and the Val Sesia Complex;
123 Quick et al., 1995; Correia et al., 2012; Mazzucchelli et al., 2014 and references therein), providing
124 evidence of a different geological evolution (Zanetti et al., 2013, 2014, 2016; Langone et al., 2017,
125 2018). In particular, the FPP has been completely recrystallised by several events of migrating melts
126 with crustal affinity (Zanetti et al., 1999; 2016; Mazzucchelli et al., 2014 and references therein),
127 and the relationships with the parental melts of the surrounding Mafic Complex are far from being
128 understood (Giovanardi et al., 2014). Conversely, the peridotites cropping out in the central and
129 southern part of IVZ did not undergo similar melt-induced recrystallisation and were emplaced in

130 the Kinzigite Formation as tectonic slivers before the intrusion of the central and southern Mafic
131 Complex (Quick et al., 1995; Mazzucchelli et al., 2014 and references therein).

132 The FPP is mainly represented by phlogopite-bearing amphibole harzburgites and associated
133 phlogopite-bearing pyroxenites (Cawthorn, 1975; Siena & Coltorti, 1989; Hartmann & Wedephol,
134 1993; Zanetti et al., 1999; Raffone et al., 2006; Selverstone & Sharp, 2011; Mazzucchelli et al.,
135 2014; Giovanardi et al., 2018). These lithologies derived from pervasive metasomatism of a
136 depleted peridotite, which formed secondary orthopyroxene, amphibole, and phlogopite (Zanetti et
137 al., 1999; Tommasi et al., 2017). Channelled migration events formed dunite bodies containing
138 stratiform to podiform chromitites and, rarely, pyroxenite and hornblendite layers (Grieco et al.,
139 2001, 2004; Zanetti et al., 2016).

140 Late stages of porous-flow melt migrations crystallised apatite- and dolomite-bearing wehrlites and
141 apatite-rich, orthopyroxene-bearing peridotites, which sometimes contain carbonate-bearing
142 domains showing marked modal and geochemical gradients with the host rocks (Zanetti et al., 1999;
143 Morishita et al., 2003, 2008; Matsumoto et al., 2005; Raffone et al., 2006). U–Pb analyses on
144 apatite and isotopic noble gas data have yielded Triassic ages (Morishita et al., 2008).

145 Apatite and calcite also occur in dykes of nepheline-bearing syenites of the Triassic age, associated
146 with hornblendites (Stähle et al., 1990, 2001). An Early Jurassic U–Pb zircon age was determined
147 for an alkali pegmatite (Grieco et al., 2001).

148 The rocks of the FPP related to the main event and the dunite bodies show similar geochemical
149 features and absence of geochemical gradients. The harzburgite–pyroxenite association and the
150 chromitite and pyroxenite layers in dunite bodies are depleted in Nb and high field strength
151 elements and significantly enriched in K, Rb, Ba, Sr, and light rare earth elements (LREEs)
152 (Hartmann & Wedephol, 1993; Zanetti et al., 1999, 2016; Mazzucchelli et al., 2014). The
153 mineralogical and compositional features have been considered by several authors as evidence of
154 the role of a slab-derived crustal component in the percolating melts (Hartmann & Wedephol, 1993;
155 Mazzucchelli et al., 1995, 2016; Rivalenti et al., 1995, 2007a; Zanetti et al., 1999, 2016; Grieco et

156 al., 2001, 2004; Morishita et al., 2003, 2008; Ponce et al., 2015; and others). Thus far, a variety of
157 different geochemical components has been identified based on isotopic data. In particular, the Hf
158 (in zircon) and O (in zircon and pyroxene) isotopic compositions of chromitites suggest the
159 presence of large volumes of continental crust in the migrating melts (Zanetti et al., 2016; Malitch
160 et al., 2017), whereas the hydrogen, oxygen, and chlorine isotopic compositions of amphibole and
161 phlogopite from the harzburgite-pyroxenite association show variability (δD from -29 to -86% ,
162 $\delta^{18}O$ from 4.9 to 6.1% , and $\delta^{37}Cl$ from -2.0 to $+2.1\%$) consistent with mixtures of magmatic fluids
163 contaminated by seawater (Hartmann & Wedepohl, 1993; Selverstone & Sharp, 2011).
164 Giovanardi et al. (2013) reported the occurrence in the FPP of late sapphirine-bearing gabbroic
165 dykes. These dykes crosscut at high angles the pervasive mantle foliation and other lithologies,
166 showing different mineralogical and major element mineral chemistry features with respect to other
167 FPP rocks.

169 **3. Samples and petrography**

170 Two different dykes and their host peridotites from the FPP unit were investigated. The first dike
171 (sample FI09C06, Fig. 2) was collected along the road that connects National Road 631 to a
172 peridotite quarry located on the right flank of the Rio Creves valley (less than 100 m from the
173 outcrops studied by Zanetti et al., 1999). The second dike (sample FI9664) is from a boulder along
174 the Rio Creves, about 30 m upstream of its intersection with the Rio Cannobino. The host peridotite
175 was collected 8 cm from the FI09C06 dyke, and close to the contact with the dyke represented by
176 sample FI9664.

177 The gabbroic dykes are centimetric in thickness (mostly 2–5 cm; Fig. 2). They show variable
178 strikes, usually crosscutting the harzburgite-pyroxenite association at high angles (Fig. 2).

179 A Mesozoic age for these sapphirine-bearing dykes is constrained by the observation that they also
180 crosscut the foliation of protomylonites in the external domains of Mesozoic shear zones (Matysiak
181 & Trepmann, 2015 and references therein), but are themselves deformed in a few cm-wide

182 mylonitic to ultramylonitic bands parallel to the protomylonite foliation (Tommasi et al., 2017).
183 Such shear zones were active at different crustal levels over a very long, Triassic–Jurassic time
184 interval (235–180 Ma; Langone et al., 2018 and references therein). This finding is also consistent
185 with the observation that all the late intrusive bodies, which are discordantly intruding the pervasive
186 mantle foliation by hydraulic fracturing, do not show ages older than Triassic (Stähle et al., 1990,
187 2001; Grieco et al., 2001; Matsumoto et al., 2005).

188 The gabbroic dykes contain sapphirine (Giovanardi et al., 2013) and show a banded symmetric
189 structure consisting of melanocratic zones at the peridotite contacts and a leucocratic zone
190 representing the dyke core (Fig. 2). The melanocratic zones, in turn, can be divided in three
191 different bands.

192 From the host peridotite to the dyke core, the following layers can be recognised:

193 1) An orthopyroxenite zone (hereafter, the Orthopyroxene Zone), established within the ambient
194 peridotite. Orthopyroxene locally shows recrystallised rims with the growth of fine neoblasts of
195 orthopyroxene and rarely olivine. The orthopyroxene sometimes presents exsolution lamellae.
196 Locally, black spinel and phlogopite occur as accessory phases. Phlogopite is concentrated in
197 interstitial positions but rarely fills fractures within orthopyroxene crystals (Fig. 2). Giovanardi et
198 al. (2013) reported the occurrence of a sapphirine- and amphibole-bearing recrystallisation front in
199 the Orthopyroxene Zone.

200 2) A first melanocratic zone (hereafter, the Early Amphibole Zone) inside veins formed by dark-
201 brown amphibole (up to 1 cm long, named 'early amphibole') and associated small plagioclase
202 grains, spinel, phlogopite, and apatite; in these zones, the magmatic texture is preserved, as
203 evidenced by amphibole twinning. Apatite and spinel mainly occur as rounded inclusions in
204 amphibole, whereas phlogopite is in interstitial position.

205 3) A second melanocratic zone (hereafter the Late Amphibole Zone), consisting of light-brown to
206 green amphibole (named 'late amphibole'), green spinel, sapphirine, and phlogopite. Sapphirine
207 occurs in three textural positions: inclusions within late amphibole, coronas rimming spinel, and

208 isolated/aggregated crystals in interstitial positions (Fig. 2). Phlogopite is an accessory phase in
209 interstitial positions. Late amphibole is smaller than early amphibole and is euhedral to anhedral in
210 shape. Intermediate green–brown amphibole, often associated with spinel and sapphirine, is
211 recognised near and through the Early Amphibole Zone–Late Amphibole Zone contact.
212 Recrystallisation zones with a fine-grained texture occur. The Late Amphibole Zone is not
213 continuous through the dykes. It forms patches, which can also occur only on one side of the
214 leucocratic core of the dyke, or that can extend up to the Orthopyroxene Zone. The Late Amphibole
215 Zone is more developed in sample FI9664 (up to about 1.5 cm in thickness) than in sample
216 FI09C06 (up to 1 cm in thickness). In addition, sapphirine crystals in sample FI9664 can reach up to
217 1.5 mm in size, whereas in sample FI09C06, they are commonly < 0.2 mm.

218 4) A leucocratic zone (Leucocratic Zone, hereafter) formed by plagioclase and subordinate
219 amphibole (both magmatic and relict from melanocratic zones). Apatite occurs as an accessory
220 phase, sometimes included in plagioclase or in relicts of brown early amphibole. The apatite rarely
221 contains calcite inclusions. Plagioclase shows twinning (mainly pericline and subordinately crossed
222 albite and pericline), which is often partially or totally erased by recrystallisation induced by late
223 deformation. Magmatic amphibole has greenish pleochroism, whereas relict amphibole, ripped from
224 the melanocratic zones, is brown. Amphibole often forms single-crystal alignments parallel to the
225 dyke strike, like in a flow texture. Phlogopite is rare and is associated with amphibole.
226 Recrystallisation zones show fine-grained equigranular texture. Rarely, Fe-oxides, Fe–Ni sulphides,
227 and pyrite occur.

228 The host peridotite away from the contact is a hornblende-harzburgite in modal composition with a
229 porphyroclastic texture (Giovanardi et al., 2018). It is characterised by the presence of olivine and
230 orthopyroxene porphyroclasts, with a secondary, undeformed mineral assemblage dominated by
231 amphibole (15% by volume), in association with orthopyroxene, spinel, phlogopite, and
232 clinopyroxene, strictly similar to the dominant peridotite type described by Zanetti et al. (1999) and
233 Tommasi et al. (2017). A detailed petrographic inspection highlights the occurrence of a reacted

peridotite zone approaching the orthopyroxene zone. It is characterised by the presence of a secondary mineral assemblage, modally dominated by long (up to 5 mm) phlogopite lamellae, with associated subordinate amounts of undeformed orthopyroxene, spinel, amphibole, and clinopyroxene. In the reacted zone, olivine was stable; conversely, the modal orthopyroxene content is slightly lower than that in the peridotite far from the vein. Primary (e.g. olivine) and secondary minerals in the reacted zones display elongation sub-parallel to the present-day vein strike.

240

241 **4. Analytical methods**

Sample FI9664, representing the gabbroic dyke and the contact host harzburgite, was analysed for whole-rock major and trace elements. Whole-rock major elements and Sc, V, Cr, Co, Ni, Cu, and Zn were analysed by X-ray fluorescence spectrometry (XRF), whereas Li, Rb, Sr, Y, Zr, Nb, Ba, rare earth element (REE), Hf, Ta, and Pb contents were analysed by inductively coupled plasma-mass spectrometry (ICP-MS). Analyses were performed following the methods described by Mazzucchelli et al. (2010) (data reported in Supplementary Material A).

Samples FI9664 and FI09C06 were analysed for mineral major elements with the electron microprobe JEOL 8200 Super Probe housed at the University of Milano. Analyses were performed following methods described by Ponce et al. (2015). Data are reported in Supplementary Material A.

Mineral trace elemental contents were determined (as in Rivalenti et al., 2007b) with a LA-ICP-MS housed at Istituto di Geoscienze e Georisorse, Consiglio Nazionale delle Ricerche, Sede Secondaria di Pavia (data are reported in Supplementary Material A) using a Perkin Elmer SCIEX DCR-e coupled with a solid-state laser source (Q-switched Nd:YAG, Quantel Brilliant). Data reduction was performed using the GLITTER software (Griffin et al., 2008). NIST SRM 610 was used as an external standard. Ca was used as an internal standard for clinopyroxene, amphibole, and plagioclase, Si for olivine, orthopyroxene, and phlogopite, and Mg for spinel. Precision and accuracy were assessed by repeated analysis of the standard BCR-2g and were found to be better

260 than 10% at the ppm concentration level. Further information is reported by Giovanardi et al.
261 (2017).

262 Sample FI09C06 was selected for O, Nd, and Sr isotopic analyses in mineral separates, after the
263 combination of preliminary electron microprobe and LA-ICP-MS analyses suggested a more
264 primitive nature for its parental melt.

265 O isotopes of pure mineral separates from sample FI09C06 were analysed at the I.G.G.-C.N.R.,
266 Pisa, by conventional laser fluorination with a Finnigan Delta Plus mass spectrometer. For each
267 phase, 1–1.5 mg aliquots were necessary to measure the oxygen isotope composition. Analyses
268 were performed following the methods described by Perinelli et al. (2011). Data are reported in
269 Table 1.

270 Sr and Nd isotopic ratios of amphibole and plagioclase separates from sample FI09C06 and the host
271 harzburgite were analysed at the Marine Environmental Sciences Laboratory (LEMAR) of the
272 Institut Universitaire Européen de la Mer (IUEM), Université de Bretagne Occidentale. Analyses
273 were carried out after dissolution and chromatographic separation using a TRITON Thermo-
274 Ionisation Mass Spectrometer (TIMS), following the procedure described by Janin et al. (2012).
275 Analyses were corrected for the reference material NBS987 ($^{87}\text{Sr}/^{86}\text{Sr} = 0.710241 \pm 0.000019$, $n =$
276 6) for Sr and the La Jolla standard ($^{143}\text{Nd}/^{144}\text{Nd} = 0.511847 \pm 0.000009$, $n = 3$) for Nd. Data are
277 reported in Table 2.

278

279 **5. Bulk rock chemistry**

280 The gabbroic dyke FI9664 presents higher TiO_2 , Al_2O_3 , CaO , Na_2O , and K_2O contents and lower
281 FeO and MgO contents than the host harzburgite collected at the contact.

282 The gabbroic dyke has trace element abundances that are one order of magnitude higher than those
283 of the host harzburgite; only Rb and Li contents are similar in both rocks (Fig. 3; Supplementary
284 Material A). The two rock types show some similarities in element fractionation: marked
285 enrichments in LREEs with respect to middle-heavy rare earth elements (M-HREE; $(\text{La}/\text{Yb})_{\text{N}}$

values are 5.5 and 16–30 for the dyke and host harzburgite, respectively; primitive mantle data from McDonough and Sun, 1995); (Th/U)_N and (Zr/Hf)_N always < 1; and positive Ba and Pb anomalies. Conversely, the (Nb/Ta)_N values are 1.6 for the gabbroic dyke and 0.7 for the host harzburgite. Linearly fractionated LREE-enriched patterns were also shown by the nepheline-bearing alkaline dykes described by Stähle et al. (2001). However, the latter had significantly higher trace element contents than those of gabbroic dyke FI9664. The dykes reported by Stähle et al. (2001) also displayed significant peculiarities in terms of fractionation of highly incompatible trace elements, such as U, Th, Nb, Ta, Ba, and Pb, with respect to REEs. The spidergram of the peridotite close to the contact with dike FI9664 shows some relevant differences with respect to those reported by Hartmann & Wedephol (1993): large positive Pb and Hf anomalies, greater Rb, U, Ba, Ta, and Nb contents, and slightly lower LREE contents (Fig. 3).

297

298 **6. Major element mineral chemistry**

299 *6.1. Host harzburgites*

The mineral composition of the host harzburgite far from the veins is similar to that of the harzburgite-pyroxenite association reported by Zanetti et al. (1999). The amphibole is pargasitic in composition, with only one analysis of Mg-hornblende composition. The mica is phlogopite, and the clinopyroxene is diopside.

Minor differences include a slightly Fe-enriched composition shown by olivine ($Fo = 100 \times \text{Mg}/(\text{Mg} + \text{Fe}^{2+}_{\text{tot}})$, molar ratio of 90.4–91.1), orthopyroxene, spinel, and amphibole (Fig. 4). Orthopyroxene and spinel (hercynite to spinel in composition) are also richer in Al. Because of their low Cr#, the FI09C06 oxides straddle the hercynite–spinel boundary, whereas oxides in the FPP are chromite. Lower Cr content is shown by amphibole, which is also characterised by lower Na and higher K contents.

At the contact with the vein, the Mg# does not change significantly in the minerals. Aluminium decreases in orthopyroxene, spinel, amphibole, and phlogopite, whereas Ti content is higher in both

312 amphibole and phlogopite. In amphibole, Na decreases, balanced by higher K content (Fig. 5).
313 Conversely, the Na/K ratio is very variable in phlogopite.
314 Orthopyroxene from the Orthopyroxene Zone has lower Mg# and CaO content and higher Al₂O₃
315 content (Fig. 4). Similarly, its composition is different from orthopyroxene from the sapphirine-
316 bearing rock found in the LIZ northern unit of the Finero Mafic Complex by Sills et al. (1983). The
317 latter has lower Mg# and higher Al₂O₃ content (Fig. 4).

318

319 6.2. Gabbroic dykes

320 Notwithstanding the similar internal banding, the two studied dykes show marked differences in
321 terms of major elemental mineral chemistry. Significant compositional changes are also shown for
322 the different types of amphibole (i.e. the Early and Late Amphibole Zones and the Leucocratic
323 Zone; Fig. 6). The unique common feature of the amphiboles of both gabbroic dykes is the higher
324 Al content exhibited by the late amphibole (Giovanardi et al., 2013). Amphibole from gabbroic
325 dykes is mostly pargasitic in composition (unit formula calculated according to Ridolfi et al., 2018),
326 but sometimes Al substitution for Si in late amphibole is higher than 2 a.p.f.u., thereby entering the
327 sadaganaite compositional field.

328 In particular, amphibole from sample FI09C06 has distinctly lower Mg# (0.73–0.82) than sample
329 FI9664 (0.85–0.87). In sample FI09C06, Mg# is lower in early amphibole than in late and
330 leucocratic amphibole, whereas it is exactly the reverse in sample FI9664 (Fig. 6).

331 FI09C06 amphibole also displays the lowest CaO and Na₂O and the highest TiO₂ and K₂O contents
332 (TiO₂ 0.27–2.19 wt.% and K₂O 0.31–1.28 wt.% respectively) (Fig. 6).

333 In sample FI09C06, TiO₂ linearly increases with the decrease in Mg#. Instead, TiO₂ is higher in the
334 FI9664 early amphibole than in the leucocratic amphibole, but distinctly higher TiO₂ contents are
335 shown by late amphibole. Moreover, in sample FI9664 early amphibole, the increase in Mg# is
336 associated with increasing Cr and Ca, and with decrease in Na and Al contents.

337 As a whole, amphibole from the gabbroic dykes has higher Al_2O_3 content and lower Mg# and Cr_2O_3
338 content with respect to others FPP lithologies, resulting in similarity to the amphibole from the
339 sapphirine-bearing rock in the LIZ (Sills et al., 1983) (Fig. 6). Amphibole from the two gabbroic-
340 dykes samples shows lower CaO and K_2O and higher Na_2O contents than the respective host
341 amphibole (Fig. 6).

342 Phlogopite from sample FI9664 presents a narrow range of major elemental contents with respect to
343 sample FI09C06. In sample FI9664, phlogopite has higher Mg# values than phlogopite from sample
344 FI09C06 (0.92–0.94 and 0.70–0.90, respectively) and commonly lower TiO_2 contents (Fig. 5).
345 Phlogopite from the gabbroic dykes shows higher Al_2O_3 content and lower Mg# than the phlogopite
346 from the host peridotite and the harzburgite-pyroxenite association (Fig. 5).

347 Spinel is mainly found in the Late Amphibole Zone. Unlike the spinel from the host harzburgite, the
348 harzburgite-pyroxenite association reported by Zanetti et al. (1999), and the chromitite layers in
349 dunite bodies (Grieco et al., 2001; 2004; Zanetti et al., 2016), the spinel from the gabbroic dykes
350 does not contain Cr_2O_3 and can be classified as spinel (Mg# 0.46–0.75).

351 Plagioclase from sample FI9664 is commonly more anorthitic than the plagioclase from sample
352 FI09C06 (An contents of 82–93 and 36–87, respectively). In both samples, some reversely zoned
353 plagioclases are recognised.

354 The sapphirine composition falls near the 7:9:3 composition on the SiO_2 –($\text{FeO} + \text{MgO}$)–($\text{Al}_2\text{O}_3 +$
355 $\text{Cr}_2\text{O}_3 + \text{Fe}_2\text{O}_3$) diagram (Fig. 7). Sapphirine from sample FI9664 is higher in Al_2O_3 content with
356 respect to sample FI09C06, whereas it is lower in SiO_2 content.

357 Scanning electron microscope (SEM) investigations at the Centro Interdipartimentale Grandi
358 Strumenti laboratories of the Università di Modena e Reggio Emilia, performed with an
359 Environmental SEM Quanta-200 (Fei Company-Oxford Instruments), suggest that apatites from
360 different zones of the dykes are Cl-apatites.

361

362 7. Trace elemental compositions

363 7.1. *Host harzburgite*

364 Amphibole and clinopyroxene from harzburgite FI09C06, 8 cm away from the contact with the
365 gabbroic dyke, are characterised by LREE-enriched linearly fractionated patterns (Figs. 8, 9 and
366 10). Their compositions are similar to those of the FPP harzburgite-pyroxenite association (Zanetti
367 et al., 1999). Proceeding toward the contact (i.e. sample FI9664), amphibole and clinopyroxene
368 show upward-convex REE patterns characterised by high variability in absolute contents (Figs. 8, 9
369 and 10). These patterns are similar to those from apatite-rich domains reported by Zanetti et al.
370 (1999) (Figs. 9 and 10).

371

372 7.2. *Gabbroic dykes*

373 The two gabbroic dykes show different trace element compositions. In sample FI09C06,
374 amphiboles from the Early Amphibole Zone and Leucocratic Zone have L-MREE-enriched
375 upward-convex patterns, similar to those of harzburgite near the contact (Fig. 8). In the Late
376 Amphibole Zone, some crystals show more fractionated patterns characterised by lower M-HREE
377 contents and positive Eu anomalies (Fig. 8). These variations are associated with marked depletion
378 in Ta, Zr, Hf, Y, Sc and V (Fig. 10, V is not shown). As a whole, amphiboles from different zones
379 of sample FI9664 show more fractionated REE patterns characterised by enrichment in LREEs and
380 depletion in HREEs (Fig. 8) with a nearly flat pattern in the LREE region. Amphibole from the
381 Early Amphibole Zone of sample FI9664 presents a small positive Eu anomaly ($(\text{Eu}/\text{Eu}^*)_{\text{N}}$ within
382 1.04–1.65), which becomes more evident in the amphibole from the Late Amphibole Zone
383 ($(\text{Eu}/\text{Eu}^*)_{\text{N}}$ within 1.29–1.62). Amphibole from sample FI9664 is also more enriched in Th, U, and
384 Pb (and to lesser extent in Sr) compared with amphibole from sample FI09C06 (Fig. 10).
385 Similar to the amphibole, REE patterns of plagioclase from sample FI9664 are more fractionated
386 than those of plagioclase from sample FI09C06, (Fig. 8). In both samples, the trace elemental
387 abundances of the plagioclase cores are greater than those of the plagioclase rims.

388 Apatite displays the typical LREE enrichment and high Th, U and Pb contents (12.31–17.35 ppm,
389 4.35–5.92 ppm, and 2.18–4.19 ppm, respectively). Nb, Ta, Zr, Hf, Ti, and Sc show negative
390 anomalies with values that are often below the detection limit.

391 No systematic trace elemental variations were found in phlogopite.

392

393 **8. O isotopes**

394 The $\delta^{18}\text{O}$ in silicates of sample FI09C06 shows a steady increase from the contact (Orthopyroxene
395 Zone) to the leucocratic gabbro in the vein core, through the Early and Late Amphibole Zones (Fig.
396 8, 10, and 11 and Table 1). In particular, it varies from 5.81‰ (standard deviation (std. dev.) 0.11)
397 in orthopyroxene from the Orthopyroxene Zone to 6.9‰ (std. dev. 0.05) in amphibole from the
398 Early and Late Amphibole Zones, and to 8.60‰ (std. dev. 0.01) in the plagioclase of the gabbroic
399 core.

400 The $\delta^{18}\text{O}$ values of orthopyroxene from the Orthopyroxene Zone lie within the mantle range. They
401 are higher than the $\delta^{18}\text{O}$ value reported by Hartmann & Wedephol (1993) for clinopyroxene from
402 the phlogopite-bearing amphibole harzburgite (Fig. 11), and for orthopyroxene from olivine-
403 chromitites of the FPP, but significantly lower than the orthopyroxene from orthopyroxene-
404 chromitites (Zanetti et al., 2016).

405 Vein amphibole and plagioclase have $\delta^{18}\text{O}$ values significantly higher than the mantle range (Fig.
406 11). They are close to the highest values found in amphibole, phlogopite, orthopyroxene,
407 clinopyroxene, and zircon from the phlogopite-bearing amphibole harzburgite-pyroxenites
408 (Hartmann & Wedephol, 1993; Selverstone and Sharp, 2011) and chromitite layers of the FPP
409 (Zanetti et al., 2016).

410 The $\delta^{18}\text{O}$ values obtained for the green spinel associated with sapphirine are markedly lower than
411 those of the associated late amphibole ($\delta^{18}\text{O} = 4.38\text{‰}$, std. dev. 0.10), as expected based on crystal-
412 chemical constraints (see Bindeman, 2008 and references therein).

413

414 9. Sr and Nd isotopes

415 The trace elemental concentrations of the mineral separates of early and late amphibole match the
416 differences highlighted by LA-ICP-MS analysis of thin sections. The Sr and Nd isotopic
417 compositions of early amphibole and late amphibole from the FI09C06 dyke are coincident within
418 analytical uncertainty (Table 2). Plagioclase from the FI09C06 Leucocratic Zone shows the same Sr
419 isotopic composition of the amphiboles, and only a slightly more radiogenic $^{143}\text{Nd}/^{144}\text{Nd}$ ratio.
420 Similar Sr isotopic compositions were documented in amphibole and apatite of discordant veins
421 from the FPP, which were characterised by higher $^{143}\text{Nd}/^{144}\text{Nd}$ ratios (Morishita et al., 2008). The
422 isotopic composition of the dyke minerals is enriched with respect to the depleted mantle reference
423 value and the mid-oceanic ridge basalt (MORB) field; these minerals fall within the ocean island
424 basalt (OIB) field (Fig. 12). In particular, they lie between the isotopic compositions of FPP
425 hornblende-syenite dykes (bulk rock from Stähle et al., 1990, 2001) and peridotites (amphibole and
426 clinopyroxene from Obermiller, 1994). Amphiboles separated from the host harzburgite (collected
427 far from the contact) show the most radiogenic Sr and unradiogenic Nd values, but have never
428 before been documented in the literature for FPP rocks (Fig. 12).

429

430 10. Discussion

431

432 10.1. Petrogenesis of the sapphirine-bearing gabbroic dykes

433 The two veins studied here share exactly the same internal banding as the sample described by
434 Giovanardi et al. (2013). This suggests that all three veins were part of an interconnected swarm,
435 which allowed them to record the same sequence of petrologic events. The symmetric structure of
436 the dykes suggests that the intrusion occurred through several events of melt percolation. In the
437 following section, we discuss, in detail, the different stages and processes that produced the
438 gabbroic dyke swarm.

439

440 *10.1.1. Melt percolation through the peridotite*

441 According to the process governing the emplacement of other dyke swarms in mantle sectors (e.g.
442 Mazzucchelli et al., 2010 and references therein), the melts flowing in the metasomatic haloes and
443 in the conduit were originally similar, undergoing severe fractionation owing to assimilation and
444 fractional crystallisation.

445 The characterisation of the wall peridotite has revealed some peculiarities. It is a common
446 observation that metasomatic haloes of cm-to-m-scale surround late dykes and veins formed by
447 melt segregation under mantle conditions. In most cases, the metasomatic haloes show marked
448 geochemical and mineralogical gradients as a function of the distance from the dike contact (Zanetti
449 et al., 1999; Ionov et al., 2002, Mazzucchelli et al., 2010; Borghini et al., 2016, 2017), which are
450 interpreted as the result of porous flow percolation of melt escaping from the open conduits.
451 Conversely, no progressive mineralogical or compositional variation is documented in the wall
452 peridotite of sample FI9664 at a variable distance from the vein (see Supplementary Material B).
453 Newly-formed clinopyroxene actually shows trace element heterogeneities, but these are randomly
454 distributed. Conversely, the trace element composition of amphibole is very homogeneous,
455 indicating late crystallisation from a unique melt.

456 The particular L/MREE-enriched convex-upward patterns shown by clinopyroxene and amphibole
457 from the wall peridotite of sample FI9664 also demonstrate that their parental melt could not have
458 been the same as that from which the adjacent early amphibole of dyke FI9664 crystallised (which
459 show linearly-fractionated REE patterns). However, based on the amphibole trace element
460 composition, the melt recorded by the wall peridotite of sample FI9664 must have been quite
461 similar to the melt that produced the Early Amphibole Zone of dyke FI09C06.

462 The textural evidence that primary and secondary minerals from the metasomatic haloes display
463 elongation sub-parallel to the present-day vein strike confirms that the development of melt
464 migration channels was associated with some local deformation.

465 These observations can be reconciled by assuming that the metasomatic haloes were not produced
466 by melt escaping normally from the conduit. They were likely established during an early stage of
467 melt migration via focused porous flow along channels developed in correspondence with structural
468 weakness, with a direction roughly parallel to the strike of the present-day veins.

469 The absence of resorption textures in olivine of the reacted wall peridotite indicates that this mineral
470 was stable. Conversely, the modal content of orthopyroxene is slightly lower than in the peridotite
471 far from the vein. This evidence leads us to consider that the orthopyroxene saturation of the melts,
472 indicated by the segregation of the reactive Orthopyroxene Zone and the presence of few
473 orthopyroxenes in the veins (Giovanardi et al., 2013), was not a clear, primary characteristic, but
474 possibly a consequence of an early stage of reactive melt migration characterised by olivine
475 precipitation and orthopyroxene dissolution (see Piccardo et al., 2017).

476 The mineralogical mismatch between the nearly monomineralic, hydrous-mineral-free
477 Orthopyroxene Zone and the Early Amphibole Zone suggests that they were segregated by
478 compositionally different melts. This hypothesis is confirmed by large differences in terms of O
479 isotopic compositions recorded by the orthopyroxene (5.8‰ standard mean ocean water (SMOW))
480 from the Orthopyroxene Zone and the amphibole from the Early Amphibole Zone (6.9‰ SMOW)
481 within the vein. The lighter O isotopic composition of the Orthopyroxene Zone would support a
482 hybrid composition of its parental melt caused by reactive porous flow through the FPP, with
483 buffering of O isotopic composition at mantle values.

484 This conclusion led us to consider the possibility that the Orthopyroxene Zone formed before the
485 segregation of the Amphibole Zones, possibly at the centre of the migration channels, as observed
486 elsewhere in the FPP. It was successively split into two parts by the opening of the fracture.

487

488 *10.1.2. Melt segregation in the open conduit*

489 The Early Amphibole Zone was segregated when melts started flowing in open fractures. It is likely
490 that amphibole crystallisation was triggered by the presence of an ultramafic wall, suggesting that

491 plagioclase was unstable in contact with the orthopyroxenite layers. The development of
492 amphibole-rich selvages where hydrous gabbroic rocks come in contact with ultramafic layers (e.g.
493 in the LIZ of the Finero Complex; Mazzucchelli et al., 2014) has previously been documented in the
494 literature.

495 The two gabbroic dykes of this study show significant differences in terms of major and trace
496 element mineral compositions. In particular, amphibole from the FI9664 vein shows an unusual
497 relative enrichment in highly incompatible trace elements (U, Th, LREEs, and Na) and compatible
498 elements (Mg, Ca, and Cr) with respect to those from the FI09C06 vein. Consistently, phlogopite is
499 more enriched in Mg and Na, and plagioclase is more anorthitic. Assuming that the dyke swarm
500 was produced by the injection of a unique melt, this relationship cannot be reconciled based on a
501 melt evolution governed only by fractional crystallisation. Mazzucchelli et al. (2010) documented
502 the same correlation between compatible and incompatible elements in minerals from cm-thick
503 diorite dykes, demonstrating that such geochemical features can be modelled considering an
504 assimilation of host minerals concomitant with fractional crystallisation (i.e. assimilation and
505 fractional crystallisation (AFC) processes). Accordingly, we argue that the parental melt of vein
506 minerals in sample FI9664 can be considered more evolved through AFC processes than that of
507 dyke FI09C06. The concomitant enrichment of Na and Ca in the vein minerals of sample FI9664
508 evidences the role of amphibole in the assimilated component. This is also confirmed by the trace
509 element patterns of FI9664 vein amphiboles, in which highly incompatible elements (such as
510 LREEs, Th, and U) increase and moderately incompatible element (such as HREEs, Ti, and Y)
511 decrease, moving toward the fractionation shown by those of host harzburgite away from the
512 contact. The decrease of moderately incompatible elements with the progression of the melt
513 evolution may be indicative of $D^{\text{Amphibole/L}}$ higher than 1 (Tiepolo et al., 2007). It is noteworthy that
514 the Al content in sample FI9664 early amphibole is comparable with to slightly lower than in those
515 from the FI09C06 vein, suggesting that the assimilation of host minerals was not effective in
516 boosting the Al concentration of the evolving melt.

517

518 *10.1.3. Formation of sapphirine-bearing patches*

519 The mm-to-cm-thick sapphirine-bearing patches and stripes are randomly distributed from the
520 internal end of the hornblendite seam to the Orthopyroxene Zone, although they are generally
521 concentrated towards the centres of the veins. They are apparently the results of interstitial
522 migration of a melt in chemical disequilibrium with the early cumulus minerals, as indicated by the
523 recrystallisation fronts inside large early amphiboles. Both interstitial and recrystallised patches
524 show that the injected melt was saturated in late amphibole, sapphirine, and spinel, whereas the
525 saturation in phlogopite is uncertain, because it occurs only interstitially and the textural
526 relationships are equivocal.

527 The following series of petrographic and geochemical features suggest that the sapphirine-bearing
528 mineral assemblages were not simply related to interaction with the parental melt of the Leucocratic
529 Zone, but were segregated because of the injection in the dyke swarm of an additional melt
530 component coming from outside the system:

- 531 1) Early amphibole at the contact with or embedded by the plagioclase of the Leucocratic Zone
532 does not show any evidence of comparable reaction.
- 533 2) Notwithstanding the significantly different major elemental composition of early amphibole
534 documented in the two veins of this study, the major elemental chemistry of sapphirine-
535 associated late amphibole converges toward specific Al and Mg# values. Phlogopite shows
536 consistent variation, even though its attribution to early or late amphibole assemblages is
537 doubtful because of its interstitial position. The data reported by Giovanardi et al. (2013)
538 confirm this trend. This finding indicates that a unique component with a specific
539 composition was responsible for the sapphirine segregation in the three sectors of the dyke
540 swarm.
- 541 3) Normalised patterns of late amphibole from sapphirine-bearing areas show particular
542 features: stronger LREE/HREE fractionation, depletion in M-HREEs, Zr, Hf, Nb, Ta, Ti, Sc,

and V, and the appearance of a positive Eu anomaly. The results also show inversion of the (Zr/Hf)_N values, which are > 1 in the early amphibole, but < 1 in the late amphibole. The overall fractionation mimics that normally exhibited by plagioclase.

The latter evidence, consistent with the apparent increase of the Al content in the system, suggests that the injected melt was characterised by a high normative plagioclase content.

The O, Nd, and Sr isotopic compositions of early and late Amphibole are very similar, suggesting that the plagioclase component belonged to the same magmatic cycle that produced the dyke swarm.

However, petrographic surveying has not provided evidence of plagioclase assimilation and/or replacement by amphibole or another mineral, excluding plagioclase components derived by local assimilation. Thus, we suggest that the plagioclase signature was acquired by the injected melt through assimilation of cumulus plagioclase in hidden magmatic bodies and/or addition in the melt source, where it was likely present as a high-P metamorphic equivalent of pristine plagioclase.

10.1.4. Segregation of the Leucocratic Zone

The petrographic evidence confirms that the formation of the Leucocratic Zone was a high energy event, which determined the partial disaggregation of the Early Amphibole Zone, with evident breaking of large early amphibole crystals. It can be locally recognised that two parts of a formerly unique crystal apparently lie on different sides of a vein. Giovanardi et al. (2013) suggested that this stage was accompanied by enlargement of the conduits.

The Nd and Sr isotopic compositions of the plagioclase indicate that the parental melt had a cognate origin with those of the hornblendite selvages. This inference is also confirmed by the trace element composition of the leucocratic amphibole, which is strictly similar to that of the associated early amphibole.

567 Nevertheless, the observation that the major elemental chemistry of the leucocratic amphibole is
568 intermediate between that of early and late amphibole leads us to conclude that the parental melt of
569 the sapphirine-bearing assemblages could be still present in diluted proportions.

570

571 *10.2. Nature of the parental melts*

572 Evaluating the nature of the parental melt of magmatic segregates belonging to narrow, cm-thick
573 veins/dykes intruding mantle peridotites at high-T-P mantle conditions must be done with particular
574 caution, with an effort first to characterise the modifications imparted by fractional crystallisation
575 and the reaction/assimilation processes with the host rock (e.g. Mazzucchelli et al., 2010 and
576 references therein). As discussed in the previous section, sample FI09C06 shows that its parental
577 melt underwent the lowest degree of interaction with the host peridotite among the known dykes,
578 and thus is the best candidate to obtain constraints on the nature of the parental melts.

579 An important contribution in defining the geochemical components in the melts is provided by the
580 marked zoning in terms of O isotopic composition documented in sample FI09C06 between the
581 Orthopyroxene Zone, the hornblende selvage, and the Leucocratic Zone.

582 The $\delta^{18}\text{O}$ values of early and late amphibole (6.9‰ SMOW) well exceed the mantle range
583 (Bindeman, 2008; Polat et al., 2018), suggesting a large contribution by crustal components in the
584 parental melt of sample FI09C06 hornblende. The proportion of the crustal component is even
585 larger in the leucocratic band, in which a $\delta^{18}\text{O}$ value of 7.8‰ SMOW can be calculated for the
586 amphibole in hypothetical equilibrium with the plagioclase composition (8.6‰ SMOW). This is
587 done by conservatively considering a low closure T for the FPP of ~850 °C (provided by pyroxene-
588 solvus geothermometry), an average value of An70 for plagioclase, and the $\delta^{18}\text{O}$ mineral
589 fractionation values reported by Bindeman (2008).

590 Published data on FPP minerals show a pronounced heterogeneity of the O isotopic composition,
591 with $\delta^{18}\text{O}$ values from below to well above the mantle range (Hartmann and Wedephol, 1993;

592 Selverstone and Sharp, 2011; Zanetti et al., 2016). This heterogeneity may be due to multiple melt-
593 migration events.

594 Values of $\delta^{18}\text{O}$ approaching those of early and late amphibole have sometimes been documented in
595 harzburgites and chromitites (Hartmann & Wedephol, 1993; Zanetti et al., 2016), but the values of
596 the leucocratic layers are markedly out of range.

597 In addition, the $\delta^{18}\text{O}$ value shown by orthopyroxene (5.81‰ SMOW) from the Orthopyroxene Zone
598 provides a very important constraint, indicating how migrating melts, after prolonged interaction
599 with the FPP, may have oxygen isotopic compositions buffered to mantle values. The decrease of
600 $\delta^{18}\text{O}$ values in the minerals from the hornblendite selvages with respect to those from the dyke core
601 (i.e. the Leucocratic Zone) confirms such a buffering effect.

602 We conclude that the high $\delta^{18}\text{O}$ shown by dyke minerals cannot be the result of interaction between
603 melts and the FPP but is a primary feature of the melts, which indicates the occurrence of large
604 amounts of crustal components, either added to the melt in the source regions or at greater mantle
605 depths.

606 A subduction-related component was identified based on noble gas isotopic composition in Late
607 Triassic apatite-rich layers (Matsumoto et al., 2005, Morishita et al., 2003, 2008), overprinting the
608 crustal affinity of the host FPP. Amphiboles from such apatite layers show the same radiogenic Sr
609 isotopic composition as the minerals of sample FI09C06, coupled to a slighter more radiogenic Nd
610 isotopic composition.

611 The isotopic compositions of early amphibole, late amphibole, and plagioclase from the FI09C06
612 dyke are significantly richer in radiogenic Sr and unradiogenic Nd isotopes compared with those
613 reported from nepheline-bearing Triassic intrusions cutting the FPP (Stähle et al., 1990, 2001),
614 which were interpreted as derived from alkaline melts of OIB affinity.

615 Combining data from nepheline-bearing alkaline dykes, sapphirine-bearing dykes, and the FPP, we
616 can define a trend at low radiogenic Nd and high radiogenic Sr isotopic ratios, suggesting mixing
617 between asthenospheric components (OIB, according to Stähle et al., 1990; 2001 and Schaltegger et

618 al., 2015) with materials derived from the continental crust (see compositional fields of Casetta et
619 al., 2018a). We speculate that the crustal components were located at lithospheric deep levels after
620 the Variscan orogenic cycle (e.g. Bonadiman et al., 1994) and mobilised by asthenospheric
621 magmatism. This scenario is supported by the evidence of continental crustal metasomatism
622 exhibited by mantle bodies involved in the Variscan collisional orogeny, such as the FPP, the Ulten
623 Zone (Sapienza et al., 2009), and some of the Bohemian Massif (Becker et al., 1999; Schulmann et
624 al., 2014).

625 In this scenario, it can be noted that the Nd and Sr isotopic compositions of sample FI09C06 lie on
626 the mixing line between the composition of the Triassic alkaline dykes and the host harzburgite
627 away from the contact. According to AFC simulation, assimilation of significant degrees of the
628 metasomatised peridotite material (15%) into OIB must be considered to account for the
629 composition of the parental melt of the FI09C06 veins.

630 Comparison of the trace elemental patterns of the amphibole from the vein apparently less
631 contaminated by the host peridotite (FI09C06) with those of amphiboles segregated by primary
632 hydrous alkaline basalts (e.g. Demeny et al., 2005) shows similarity in REE fractionation, but the
633 early amphibole has an absolute content that is nearly one order of magnitude higher. In addition, a
634 correlation with primary alkaline mantle melts is not directly supported by the negative Nb, Ta, and
635 Ti anomalies shown by the early amphibole.

636 Equilibrium liquids calculated from the trace elemental composition of early amphibole from the
637 FI09C06 dyke and amphibole-melt partition coefficients experimentally determined at 1,015 °C in
638 the presence of moderately polymerised melts (dataset T2 1015; Tiepolo et al., 2007) match the
639 REE contents and fractionation exhibited by shoshonitic rocks of the Triassic magmatism of the
640 Dolomites area (Casetta et al., 2018a; 2018b; see Supplementary Material C). The calculated melts
641 also show consistent negative Ti anomalies, $(\text{Nb/La})_N$ values close to 1, and slight positive U, Th,
642 and Pb anomalies; the latter are more pronounced in the shoshonitic melts. However, a best match
643 in terms of U, Th, and Pb concentrations is shown by equilibrium liquids calculated in equilibrium

644 with amphiboles from 9,664 dykes. These observations suggest that the sapphirine-bearing gabbroic
645 dykes may record the deep mantle input of Triassic K-rich calc-alkaline to shoshonitic melts
646 erupted into the eastern Southern Alps, also documenting the fractionation trends responsible for the
647 enrichment in Th, U, and Pb. This hypothesis is also supported by the Sr and Nd isotopic
648 compositions of Triassic K-rich calc-alkaline to shoshonitic intrusive rocks and lavas of the Eastern
649 Alps (Casetta et al., 2018a; Figure 12), which approach the isotopic trend defined by our model.

650

651 *10.3. Constraints on the geodynamic evolution of the Europe–Africa boundary*

652

653 *10.3.1. P–T constraints on the FPP*

654 Geothermobarometric estimates constrain the intrusion of sapphirine-bearing dykes at very high-P
655 and T conditions. Ab-initio calculations indicate that the primary crystallisation field of sapphirine
656 in the MAS diagram ($\text{SiO}_2\text{--MgO--Al}_2\text{O}_3$) becomes considerably larger over 1.0 GPa and shrinks at
657 2.0 GPa (Belmonte et al., 2014). This evidence confirms the experimental results of Liu & Presnall
658 (1990, 2000) and Milholland & Presnall (1998), indicating that magmatic sapphirine in FPP veins
659 likely crystallised at $P \geq 1$ GPa. Equilibrium T estimates based on the sapphirine–spinel Mg–Fe^{2+}
660 exchange thermometer of Sato et al. (2006) and the amphibole–plagioclase thermometer of Holland
661 & Blundy (1994) are mostly higher than 1,000 °C (up to 1,085 °C), confirming the T estimates of
662 Giovanardi et al. (2013). The melt T was thus significantly higher than that in the host harzburgite,
663 which shows solidus T typically corresponding to the water-oversaturated peridotite (965 °C at $P =$
664 1.1 GPa; Giovanardi et al., 2013). The absence of partial melting evidence in the host FPP confirms
665 that the source of the uprising melts was at greater mantle depths. The high T, in combination with
666 the high water and volatile contents, may have allowed the melt to migrate via porous flow along
667 the direction of structural weakness (see Tommasi et al., 2017) before the opening of the conduits.
668 The high-P emplacement conditions are consistent with the scenario where the FPP, after
669 Palaeozoic metasomatism, remained at depths greater than the large lherzolitic mantle bodies south

670 of the Anzola-Val Grande high-T shear zone (namely, from north to south, Premosello, Balmuccia,
671 and Baldissero; Quick et al., 1995), until its exhumation at shallower levels at ~180 Ma (Zanetti et
672 al., 2013, 2016; Langone et al., 2017, 2018; Decarlis et al., 2017, Malitch et al., 2017; Petri et al.,
673 2019).

674

675 *10.3.2. Constraints on the Mesozoic mantle sources at the Africa–Europe Boundary*

676 The outcomes of this study indicate that in the Mesozoic, melts extremely rich in volatiles (H₂O, P,
677 CO₂, and Cl), K, Na, and highly incompatible elements rose from mantle depths toward the surface.
678 The large crustal component present in the melts, as indicated by the O isotopic composition, leads
679 us to consider that the high Al content, enrichment in large-ion lithophile elements and LREEs, and
680 enriched Nd and Sr isotopic compositions are a primary feature inherited from the source.

681 This finding confirms the extreme complexity of the tectono-magmatic scenario recorded by the
682 FPP. In particular, the northern IVZ records an extremely prolonged release of K-H₂O-rich mantle-
683 derived melts mixed with subduction-related components, which lasted from the Variscan orogenic
684 cycle to the Mesozoic exhumation of lithospheric mantle at shallower levels. This explains why the
685 FPP records many generations of phlogopite-bearing mineral assemblages, showing variable field
686 relationships, geochemical signatures, and ages (Hartmann & Wedephol, 1993; Zanetti et al., 1999;
687 2013; 2016; Stähle et al., 1990; 2001; Greco et al., 2001; 2004; Morishita et al., 2003, 2008;
688 Malitch et al., 2017). It also provides a new interpretative frame for previous data indicating the
689 emplacement of melts with subduction-related components in the Triassic (Mastumoto et al., 2005;
690 Morishita et al., 2008, Malitch et al., 2017).

691 This magmatism-bearing subduction component appears to have roughly overlapped with the ascent
692 of silica-undersaturated alkaline melts of OIB affinity (Stähle et al., 1990, 2001, Schaltegger et al.,
693 2015), which likely also have some counterparts in the central IVZ (Fiorentini et al., 2018; Galli et
694 al., 2019).

695 The FPP developed in a concomitant extensional–transtensional tectonic regime, the origin and
696 geodynamic scenario of which are still strongly debated (Cassinis et al., 2008; Zanetti et al., 2013;
697 Casetta et al., 2018a, b). Further investigations are needed to address whether the crustal
698 components are remnants of old subduction events (Bonadiman et al., 1994), possibly located at
699 lithospheric levels, reactivated by asthenospheric magmatism with OIB or depleted mantle affinity;
700 represent crustal material recycled into asthenospheric mantle sources (Locmelis et al., 2016); or
701 were added by active Mesozoic subduction (Cassini et al., 2008; Schmid et al., 2008; Morishita et
702 al., 2008; Selverstone and Sharp, 2011; Zanetti et al., 2013).

703 It is a matter of fact that the major elements (in particular the enrichment in K and Al), trace
704 elements, and Sr and Nd isotopic compositions of the sapphirine-bearing gabbroic rocks approach
705 the geochemical affinity shown by Triassic K-rich calc-alkaline to shoshonitic magmatism of the
706 Dolomites area (Eastern Alps) (Casetta et al., 2018a, b). Thus, the study of magmatic events at the
707 roots of the continental crust of the Adria Plate can provide a unique opportunity to constrain the
708 tectono-magmatic evolution of the Europe–Africa boundary.

709

710 **11. Concluding remarks**

711 A detailed survey of Mesozoic sapphirine-bearing gabbroic dykes within the FPP unit led us to
712 recognise different stages of melt migration (from porous-flow migration in peridotite channels to
713 flow in open conduits) and constrain the presence in the parental melts of a large continental crustal
714 component acquired in the source region or at deeper lithospheric mantle levels.

715 The reaction between dyke melts and the strongly metasomatised FPP enhanced the crustal
716 signature.

717 The high Al content of these melts allowed the segregation of magmatic sapphirine, which is a
718 marker of high-P-T intrusive conditions.

719 This dyke swarm possibly represents a record of the input to the mantle of the K-rich calc-alkaline
720 to shoshonitic melts that characterised the magmatism widespread during the Triassic in the
721 Southern Alps area.

722

723 **Acknowledgements**

724 This work was supported by Ministero dell'Istruzione dell'Università e della Ricerca (MIUR),
725 Progetti di Rilevante Interesse Nazionale (PRIN) 2015 Protocol 20158A9CBM. We thank Jean
726 Yves Cottin and Dejan Prelević for their constructive comments and Elsevier Language Editing
727 Services for improving the quality of the text.

728

729

730

731

732

733

734

735

736

737

738

739

740

741

742

743 **References**

744 Becker, H., Wenzel, T., Volker, F., 1999. Geochemistry of glimmerite veins in peridotites from
 745 Lower Austria - implications for the origin of K-rich magmas in collision zones. *Journal of*
 746 *Petrology* 40, 315-338.

747 Belmonte, D., Ottonello, G., Zuccolini, M.V., 2014. Ab initio thermodynamic and thermophysical
 748 properties of sapphirine end-members in the join $\text{Mg}_4\text{Al}_8\text{Si}_2\text{O}_{20}$ - $\text{Mg}_3\text{Al}_{10}\text{SiO}_{20}$. *American*
 749 *Mineralogist* 99, 1449-1461.

750 Bindeman, I., 2008. Oxygen Isotopes in Mantle and Crustal Magmas as Revealed by Single Crystal
 751 Analysis. *Reviews in Mineralogy & Geochemistry* 69, 445-478.

752 Bonadiman, C., Coltorti, M., Siena, F., 1994. Petrogenesis and T - $f\text{O}_2$ estimates of Mt. Monzoni
 753 complex (Central Dolomites, Southern Alps): a Triassic shoshonitic intrusion in a transcurrent
 754 geodynamic setting. *European Journal of Mineralogy* 6, 943-966.

755 Borghini, G., Rampone, E., Zanetti, A., Class, C., Cipriani, A., Hofmann, A.W., Goldstein, S.L.,
 756 2016. Pyroxenite layers in the Northern Apennines' upper mantle (Italy) - generation by pyroxenite
 757 melting and melt infiltration. *Journal of Petrology* 57, 625-653.

758 Borghini, G., Fumagalli, P., Rampone E., 2017. Partial melting of secondary pyroxenite at 1 and 1.5
 759 GPa, and its role in upwelling heterogeneous mantle. *Contributions to Mineralogy and Petrology*
 760 172, 70, <https://doi.org/10.1007/s00410-017-1387-4>.

761 Casetta, F., Coltorti, M., Ickert, R.B., Bonadiman, C., Giacomoni, P.P., Ntaflos, T., 2018a. Intrusion
 762 of shoshonitic magmas at shallow crustal depth: T - P path, H_2O estimates, and AFC modeling of the
 763 Middle Triassic Predazzo Intrusive Complex (Southern Alps, Italy). *Contributions to Mineralogy*
 764 *and Petrology* 173, 57, <https://doi.org/10.1007/s00410-018-1483-0>.

765 Casetta, F., Coltorti, M., Marrocchino, E., 2018b. Petrological evolution of the Middle Triassic
 766 Predazzo Intrusive Complex, Italian Alps. *International Geology Review* 60, 977-997.

767 Cassinis, G., Cortesogno, L., Gaggero, L., Perotti, C. R., Buzzi, L., 2008. Permian to Triassic and
 768 magmatic evolution of the Brescian Prealps (eastern Lombardy, Italy). *Italian Journal of*
 769 *Geosciences* 3, 501-518.

770 Cawthorn, R.G., 1975. The Amphiboleibole peridotite - metagabbro complex, Finero, northern
771 Italy. *Journal of Geology* 83, 437-454.

772 Correia, C.T., Sinigoi, S., Girardi, V.A.V., Mazzucchelli, M., Tassinari, C.C.G., Giovanardi, T.,
773 2012. The growth of large mafic intrusions: Comparing Niquelândia and Ivrea igneous complexes.
774 *Lithos* 155, 167-182.

775 Consuma, G., Braga, R., Giovanardi, T., Bersani, D., Konzett, J., Lugli, F., Mazzucchelli, M.,
776 Tropper, P. 2019. *In situ* Sr isotope analysis of mantle carbonates: Constraints on the evolution and
777 sources of metasomatic carbon-bearing fluids in a paleo-collisional setting. *Lithos*
778 <https://doi.org/10.1016/j.lithos.2019.105334>.

779 Cumming, G.L., Köppel, V., Ferrario, A., 1987. A lead isotope study of the northeastern Ivrea Zone
780 and the adjoining Ceneri zone (N-Italy): evidence for a contaminated subcontinental mantle.
781 *Contribution to Mineralogy and Petrology* 97, 19-30.

782 Decarlis, A., Beltrando, M., Manatschal, G., Ferrando, S., Carosi, R., 2017. Architecture of the
783 distal Piedmont-Ligurian rifted margin in NW Italy: Hints for a flip of the rift system polarity.
784 *Tectonics* 36, 2388-2406.

785 Demény, A., Vennemann, T.W., Homonnay, Z., Milton, A., Embey-Isztin, A., Nagy, G., 2005.
786 Origin of amphibole megacrysts in the Pliocene-Pleistocene basalts of the Carpathian-Pannonian
787 region. *Geologica Carpathica* 56, 179-189.

788 Dohmen, R., Blundy, J., 2014. A predictive thermodynamic model for element partitioning between
789 plagioclase and melt as a function of pressure, temperature and composition. *American Journal of*
790 *Science* 314, 1319–1372.

791 Fiorentini, M.L., LaFlamme, C., Denyszyn, S., Mole, D., Maas, R., Locmelis, M., Caruso, S., Bui,
792 T.-H., 2018. Post-collisional alkaline magmatism as gateway for metal and sulfur enrichment of the
793 continental lower crust. *Geochimica et Cosmochimica Acta* 223, 175-197.

794 Galli, A., Grassi, D., Sartori, G., Gianola, O., Burg, J.-P., Schmidt, M.W., 2019. Jurassic carbonatite
795 and alkaline magmatism in the Ivrea zone (European Alps) related to the breakup of Pangea.
796 *Geology* 47, 1–4, <https://doi.org/10.1130/G45678.1>.

797 Garuti, G., Bea, F., Zaccarini, F., Montero, P., 2001. Age, geochemistry and petrogenesis of the
798 ultramafic pipes in the Ivrea Zone, NW Italy. *Journal of Petrology* 42, 433–457.

799 Giovanardi, T., Morishita, T., Zanetti, A., Mazzucchelli, M., Vannucci, R., 2013. Igneous
800 sapphirine as a product of melt-peridotite interactions in the Finero Phlogopite-Peridotite Massif,
801 Western Italian Alps. *European Journal of Mineralogy* 25, 17-31.

802 Giovanardi, T., Mazzucchelli, M., Zanetti, A., Langone, A., Tiepolo, M., Cipriani, A., 2014.
803 Occurrence of Phlogopite in the Finero Mafic Layered Complex. *Central European Journal of*
804 *Geosciences* 6 (4), 588-613.

805 Giovanardi, T., Girardi, V.A.V., Correia, C.T., Sinigoi, S., Tassinari, C.C.G., Mazzucchelli, M.,
806 2017. The growth and contamination mechanism of the Cana Brava layered mafic-ultramafic
807 complex: new field and geochemical evidences. *Mineralogy and Petrology* 111, 291-314.

808 Giovanardi, T., Freddo, I., Mazzucchelli, M., 2018. Filling the Gap in the Classification of
809 Phlogopite-Bearing Ultramafic Rocks. *The Journal of Geology* 126, 361–370.

810 Grieco, G., Ferrario, A., von Quadt, A., Köppel, V., Mathez, A., 2001. The zircon-bearing
811 chromitites of the phlogopite peridotite of Finero (Ivrea Zone, Southern Alps): evidence and
812 geochronology of a metasomatized mantle slab. *Journal of Petrology* 42/1, 89-101.

813 Grieco, G., Ferrario, A., Mathez, E.A., 2004. The effect of metasomatism on the Cr-PGE
814 mineralization in the Finero Complex, Ivrea Zone, Southern Alps. *Ore Geology Reviews* 24, 299-
815 314.

816 Griffin, W.L., O'Reilly, S.Y., 1986. Mantle-derived sapphirine. *Mineralogical Magazine* 50, 635-
817 640.

818 Griffin, W.L., Powell, W.J., Pearson, N.J., O'Reilly, S.Y., 2008. GLITTER: data reduction software
819 for laser ablation ICPBMS. In: Sylvester P. (Ed.), *Laser Ablation ICP–MS in the Earth Sciences:*

820 Current Practices and Outstanding Issues. Mineralogical Association of Canada Short Course Series
821 40, 308-311.

822 Hartmann, G., Wedepohl, K.H., 1993. The composition of peridotite tectonites from the Ivrea
823 Complex, northern Italy: Residues from melt extraction. *Geochimica et Cosmochimica Acta* 57,
824 1761-1782.

825 Higgins, J.B., Ribbe, R.H., Herd, R.K., 1979. Sapphirine I. Crystal chemical contributions.
826 *Contribution to Mineralogy and Petrology* 68, 349-356.

827 Holland, T., Blundy, J., 1994. Non-ideal interactions in calcic amphiboles and their bearing on
828 amphibole-plagioclase thermometry. *Contributions to Mineralogy and Petrology* 116, 433-447.

829 Ionov, D.A., Bodinier, J.-L., Mukasa, S.B., Zanetti, A., 2002. Mechanisms and sources of mantle
830 metasomatism: major and trace element compositions of peridotite xenoliths from Spitsbergen in
831 the context of numerical modelling. *Journal of Petrology* 43, 1-41.

832 Janin, M., Hémond, C., Maia, M., Nonnotte, P., Ponzevera, E., Johnson, K.T.M., 2012. The
833 Amsterdam–St. Paul Plateau: A complex hot spot/DUPAL-flavored MORB interaction.
834 *Geochemistry Geophysics Geosystems* 13-9, 10.1029/2012GC004165.

835 Langone, A., Padrón-Navarta, J. A., Ji, W.-Q., Zanetti, A., Mazzucchelli, M., Tiepolo, M.,
836 Giovanardi, T., Bonazzi, M., 2017. Ductile-brittle deformation effects on crystal-chemistry and U-
837 Pb ages of magmatic and metasomatic zircons from a dyke of the Finero Mafic Complex (Ivrea-
838 Verbano Zone, Italian Alps). *Lithos* 284-285, 493-511.

839 Langone, A., Zanetti, A., Daczko, N.R., Piazzolo, S., Tiepolo, M., Mazzucchelli, M., 2018. Zircon
840 U-Pb dating of a lower crustal shear zone: A case study from the northern sector of the Ivrea-
841 Verbano Zone (Val Cannobina, Italy). *Tectonics* 37, 322–342.

842 Lensch, G., 1968. Die Ultramafitite der Zone von Ivrea und ihre geologische Interpretation.
843 *Schweizerische Mineralogische Petrographische Mitteilung* 48, 91-102.

844 Liu, T.C., Presnall, D.C., 1990. Liquidus phase relationships on the join anorthite-forsterite-quartz
 845 at 20 kbar with applications to basalt petrogenesis and igneous sapphirine. *Contributions to*
 846 *Mineralogy and Petrology* 104, 735-742.

847 Liu, T.C., Presnall, D.C., 2000. Liquidus phase relations in the system CaO-MgO-Al₂O₃-SiO₂ at
 848 2.0 GPa: applications to basalt fractionation, eclogites, and igneous sapphirine. *Journal of Petrology*
 849 41, 3-20.

850 Locmelis, M., Fiorentini, M.L., Rushmer, T., Arevalo Jr, R., Adam, J., Denyszyn, S.W., 2016.
 851 Sulfur and metal fertilization of the lower continental crust. *Lithos* 244, 74-93.

852 Lu, M., Hofmann, A.W., Mazzucchelli, M., Rivalenti, G., 1997a. The mafic-ultramafic complex
 853 near Finero (Ivrea-Verbano zone), I. Chemistry of MORB-like magmas. *Chemical Geology* 140,
 854 207-222.

855 Lu, M., Hofmann, A.W., Mazzucchelli, M., Rivalenti, G., 1997b. The mafic-ultramafic complex
 856 near Finero (Ivrea-Verbano zone), II. Geochronology and isotope geochemistry. *Chemical Geology*
 857 140, 223-235.

858 Lyubetskaya, T., Korenaga, J., 2007. Chemical composition of Earth's primitive mantle and its
 859 variance: 1. Method and results. *Journal of Geophysical Research* 112, B03211.

860 Malitch, K.N., Belousova, E.A., Griffin, W.L., Badanina, I.Yu., Knauf, V.V., O'Reilly, S.Y.,
 861 Pearson, N.J., 2017. Laurite and zircon from the Finero chromitites (Italy): New insights into
 862 evolution of the subcontinental mantle: *Ore Geology Reviews* 90, 210–225.

863 Matsumoto, T., Morishita, T., Masuda, J., Fujioka, T., Takebe, M., Yamamoto, K., Arai, S., 2005.
 864 Noble gases in the Finero Phlogopite–Peridotites, Italian Western Alps. *Earth and Planetary Science*
 865 *Letters* 238, 130-145.

866 Matysiak, A.K., Trepmann, C.A., 2015. The deformation record of olivine in mylonitic peridotites
 867 from the Finero Complex, Ivrea Zone: Separate deformation cycles during exhumation. *Tectonics*
 868 34, 2514-2533.

869 Mazzucchelli, M., Rivalenti, G., Piccirillo, E.M., Girardi, V.A.V., Civetta, L., Petrini, R., 1995.
870 Petrology of the Proterozoic mafic dyke swarms of Uruguay and constraints on their mantle source
871 composition. *Precambrian Research* 74, 177-194.

872 Mazzucchelli, M., Rivalenti, G., Brunelli, D., Zanetti, A., Boari, E., 2009. Formation of highly
873 refractory dunite by focused percolation of pyroxenite-derived melt in the Balmuccia peridotite
874 Massif (Italy). *Journal of Petrology* 50, 1205-1233.

875 Mazzucchelli, M., Zanetti, A., Rivalenti, G., Vannucci, R., Correia, C.T., Tassinari, C.C.G., 2010.
876 Age and geochemistry of mantle peridotites and diorite dykes from the Baldissero body: Insights
877 into the Paleozoic-Mesozoic evolution of the Southern Alps. *Lithos* 119, 485-500.

878 Mazzucchelli, M., Quick, J.E., Sinigoi, S., Zanetti, A., Giovanardi, T., 2014. Igneous evolutions
879 across the Ivrea crustal section: The Permian Sesia Magmatic System and the Triassic Finero
880 intrusion and mantle. *Geological Field Trips* 6 (2.2), 1-98.

881 Mazzucchelli, M., Cipriani, A., Hémond, C., Zanetti, A., Bertotto, G.W., Cingolani, C.A., 2016.
882 Origin of the DUPAL anomaly in mantle xenoliths of Patagonia (Argentina) and geodynamic
883 consequences. *Lithos* 248-251, 257-271.

884 McDonough, W.F., Sun, S.-s., 1995. The composition of the Earth. *Chemical Geology* 120, 223-
885 253.

886 Milholland, C.S., Presnall, D.C., 1998. Liquidus phase relations in the CaO-MgO-Al₂O₃-SiO₂
887 system at 3.0 GPa: the Aluminous pyroxene thermal divide and high-pressure fractionation of
888 picritic and komatiitic magmas. *Journal of Petrology* 39, 3-27.

889 Morishita, T., Arai, S., Tamura, A., 2003. Petrology of an apatite-rich layer in the Finero
890 phlogopite–peridotite, Italian Western Alps; implications for evolution of a metasomatising agent.
891 *Lithos* 69, 37-49.

892 Morishita, T., Hattori, K.H., Terada, K., Matsumoto, T., Yamamoto, K., Takebe, M., Ishida, Y.,
893 Tamura, A., Arai, S., 2008. Geochemistry of apatite-rich layers in the Finero phlogopite–peridotite
894 massif (Italian Western Alps) and ion microprobe dating of apatite. *Chemical Geology*, 251 99-111.

895 Mukasa, S.B., Shervais, J.W., 1999. Growth of subcontinental lithosphere: evidence from repeated
896 dike injections in the Balmuccia lherzolite massif, Italian Alps. *Lithos* 48, 287-316

897 Obermiller, W.A., 1994. Chemical and isotopic variations in the Balmuccia, Baldissero and Finero
898 peridotite massifs (Ivrea-Zone, N-Italy). Unpublished PhD thesis, Johannes Gutenberg-Universität
899 Mainz pp. 191.

900 Perinelli, C., Armienti, P., Dallai, L., 2011. Thermal evolution of the lithosphere in a rift
901 environment as inferred from the geochemistry of mantle cumulates, Northern Victoria Land,
902 Antarctica. *Journal of Petrology* 52, 665-690.

903 Petri, B., Duretza, T., Mohn, G., Schmalholz, S.M., Karner, G.D., Müntener, O., 2019. Thinning
904 mechanisms of heterogeneous continental lithosphere. *Earth and Planetary Science Letters* 512,
905 147-162.

906 Piccardo, G.B., Zanetti, Z., Müntener, O., 2007. Melt/peridotite interaction in the Southern Lanzo
907 peridotite: field, textural and geochemical evidence. *Lithos* 94, 181-209.

908 Polat, A., Frei, R., Longstaffe, F.J., Thorkelson, D.J., Friedman, E., 2018. Petrology and
909 geochemistry of the Tasse mantle xenoliths of the Canadian Cordillera: A record of Archean to
910 Quaternary mantle growth, metasomatism, removal, and melting. *Tectonophysics* 737, 1-26.

911 Ponce, A.D., Bertotto, G.W., Zanetti, A., Brunelli, D., Giovanardi, T., Aragón, E., Bernardi, M.I.,
912 Hémond, C., Mazzucchelli, M., 2015. Short-scale variability of the SCLM beneath the extra-
913 Andean back-arc (Paso de Indios, Argentina): evidence from spinel-facies mantle xenoliths. *Open*
914 *Geosciences* 7, 362–385.

915 Princivalle, F., DeMin, A., Lenaz, D., Scarbolo, M., Zanetti, A., 2014. Ultramafic xenoliths from
916 Damaping (Hannuoba region, NE-China): Petrogenetic implications from crystal chemistry of
917 pyroxenes, olivine and Cr-spinel and trace element content of clinopyroxene. *Lithos* 188, 3-14.

918 Quick, J.E., Sinigoi, S., Mayer, A., 1995. Emplacement of mantle peridotite in the lower continental
919 crust, Ivrea-Verbano Zone, northwest Italy. *Geology* 23, 739-742.

920 Raffone, N., Le Fèvre, B. L., Ottolini, L., Vannucci, R., Zanetti, A., 2006. Light-lithophile element
 921 metasomatism of Finero peridotite (W Alps): A secondary-ion mass spectrometry study.
 922 *Microchimica Acta* 155, 251-255.

923 Ridolfi, F., Zanetti, A., Renzulli, A., Perugini, D., Holtz, F., Oberti, R., 2018. AMFORM, a new
 924 mass-based model for the calculation of the unit formula of amphiboles from electron microprobe
 925 analyses. *American Mineralogist* 103, 1112-1125.

926 Rivalenti, G., Mazzucchelli, M., Molesini, M., Petrini, R., Girardi, V.A.V., Bossi, J., Campal, N.,
 927 1995. Petrology of late proterozoic mafic dikes in the Nico Perez region, central Uruguay.
 928 *Mineralogy and Petrology* 55, 239-263.

929 Rivalenti, G., Mazzucchelli, M., Zanetti, A., Vannucci, R., Bollinger, C., Hémond, C., Bertotto,
 930 G.W., 2007a. Xenoliths from Cerro de los Chenques (Patagonia): An example of slab-related
 931 metasomatism in the backarc lithospheric mantle, *Lithos* 99, 45-67.

932 Rivalenti, G., Zanetti, A., Girardi, V.A.V., Mazzucchelli, M., Tassinari, C.C.G., Bertotto, G.W.,
 933 2007b. The effect of the Fernando de Noronha plume on the mantle lithosphere in north-eastern
 934 Brazil. *Lithos* 94, 111-131.

935 Rocco, I., Zanetti, A., Melluso, L., Morra, V., 2017. Ancient-depleted and enriched mantle
 936 lithosphere domains in northern Madagascar: geochemical and isotopic evidence from spinel-to-
 937 plagioclase-bearing ultramafic xenoliths. *Chemical Geology* 466, 70-85.

938 Rollinson, H., 1993. Using geochemical data: evaluation, presentation interpretation. Longman
 939 Group UK Ltd, 1994 reprinted, pp. 352.

940 Sapienza, G.T., Scambelluri, M., Braga, R., 2009. Dolomite-bearing orogenic garnet peridotites
 941 witness fluid-mediated carbonrecycling in a mantle wedge (Ulten Zone, Eastern Alps, Italy).
 942 *Contributions to Mineralogy and Petrology* 158, 401-420.

943 Sato, K., Miyamoto, T., Kawasaki, T., 2006. Experimental calibration of sapphirine-spinel Fe^{2+} -Mg
 944 exchange thermometer: implication for constraints on P-T condition of Howard Hills, Napier
 945 Complex, East Antarctica. *Gondwana Research* 9, 398-408.

946 Schaltegger, U., Ulianov, A., Müntener, O., Ovtcharova, M., Peytcheva, I., Vonlanthen, P.,
 947 Vennemann, T., Antognini, M., Girlanda, F., 2015. Megacrystic zircon with planar fractures in
 948 miaskite-type nepheline pegmatites formed at high pressures in the lower crust (Ivrea Zone,
 949 southern Alps, Switzerland). *American Mineralogist* 100, 83-94.

950 Schmid, S.M., Bernoulli, D., Fügenschuh, B., Matenco, L., Schefer, S., Schuster, R., Tischler, M.,
 951 Ustaszewsk, K., 2008. The Alpine-Carpathian-Dinaridic orogenic system: correlation and evolution
 952 of tectonic units. *Swiss Journal of Geosciences* 101, 139-183.

953 Schulmann, K., Lexa, O., Janoušek, V., Lardeaux, J.M., Edel, J.B., 2014. Anatomy of a diffuse
 954 cryptic suture zone: An example from the Bohemian Massif, European Variscides. *Geology* 42,
 955 275-278.

956 Seitz, H.M., Woodland, A.B., 2000. The distribution of lithium in peridotitic and pyroxenitic mantle
 957 lithologies - an indicator of magmatic and metasomatic processes. *Chemical Geology* 166, 47–64.

958 Selverstone, J., Sharp, Z.D., 2011. Chlorine isotope evidence for multicomponent mantle
 959 metasomatism in the Ivrea Zone. *Earth and Planetary Science Letters* 310, 429-440.

960 Shervais, J.W., Mukasa, S.B., 1991. The Balmuccia orogenic lherzolite massif, Italy. *Journal of*
 961 *Petrology, Special Lherzolite issue*, 155-174.

962 Siena, F., Coltorti, M., 1989. The petrogenesis of a hydrated mafic - ultramafic complex and the
 963 role of amphibole fractionation at Finero (Italian Western Alps). *Neues Jahrbuch für Mineralogie* 6,
 964 255-274.

965 Sills, J.D., Ackermann, D., Herd, R.K., Windley, B.F., 1983. Bulk composition and mineral
 966 parageneses of sapphirine-bearing rocks along a gabbro-lherzolite contact at Finero, Ivrea Zone, N
 967 Italy. *Journal of Metamorphic Geology* 1, 337-351.

968 Stälhe, V., Frenzel, G., Kober, B., Michard, A., Puchelt, H., Schneider, W., 1990. Zircon syenite
 969 pegmatites in the Finero peridotite (Ivrea Zone): evidence for a syenite from a mantle source. *Earth*
 970 *and Planetary Science Letters* 101, 196-205.

971 Stähle, V., Frenzel, G., Hess, J. C., Saupé, F., Schmidt, S. Th., Schneider, W., 2001. Permian
 972 metabasalt and Triassic alkaline dykes in the Northern Ivrea Zone: clues to the post-Variscan
 973 geodynamic evolution of the Southern Alps. *Schweizerische Mineralogische und Petrographische*
 974 *Mitteilungen* 81, 1-21.

975 Tiepolo, M., Oberti, R., Zanetti, A., Vannucci, R., Foley, S.F., 2007. Trace-Element partitioning
 976 between Amphibole and silicate melt. *Reviews in Mineralogy and Geochemistry* 67, 417-452.

977 Tommasi, A., Langone, A., Padrón-Navarta, J. A., Zanetti, A., Vauchez, A., 2017. Hydrous melts
 978 weaken the mantle, crystallization of pargasite and phlogopite does not: Insights from a
 979 petrostructural study of the Finero peridotites, Southern Alps. *Earth and Planetary Science Letters*
 980 477, 59–72.

981 Voshage, H., Hunziker, J.C., Hofmann, A.W., Zingg, A., 1987. A Nd and Sr isotopic study of the
 982 Ivrea zone, Southern Alps, N-Italy. *Contributions to Mineralogy and Petrology* 97, 31–42.

983 Voshage, H., Sinigoi, S., Mazzucchelli, M., Demarchi, G., Rivalenti, G., Hofmann, A.W., 1988.
 984 Isotopic constraints on the origin of ultramafic and mafic dikes in the Balmuccia peridotite (Ivrea
 985 Zone). *Contributions to Mineralogy and Petrology* 100 (3), 261–267.

986 Workman, R.K., Hart, S.R., 2005) Major and trace element composition of the depleted MORB
 987 mantle (DMM). *Earth Planetary Science Letter* 231, 53–72.

988 Zaccarini, F., Stumpfl, E.F., Garuti, G., 2004. Zirconolite and Zr–Th–U minerals in chromitites of
 989 the Finero complex, Western Alps, Italy: evidence for carbonatite type metasomatism in a
 990 subcontinental mantle plume. *The Canadian Mineralogist* 42, 1825–1845.

991 Zanetti, A., Mazzucchelli, M., Rivalenti, G., Vannucci, R., 1999. The Finero phlogopite-peridotite
 992 massif: an example of subduction-related metasomatism. *Contributions to Mineralogy and*
 993 *Petrology* 134, 107-122.

994 Zanetti, A., Mazzucchelli, M., Sinigoi, S., Giovanardi, T., Peressini, G., Fanning, M., 2013. Insights
 995 into the Melt-Lower Crust Interplay in Subduction-related Setting and the Mesozoic Geodynamic

996 Evolution of the Southern Alps: evidence from the Finero Mafic Complex (Ivrea-Verbano Zone).
997 Journal of Petrology 54, 2235-2265.
998 Zanetti, A., Mazzucchelli, M., Sinigoi, S., Giovanardi, T., Peressini, G., Fanning, M., 2014.
999 Erratum Insights into the Melt-Lower Crust Interplay in Subduction-related Setting and the
1000 Mesozoic Geodynamic Evolution of the Southern Alps: evidence from the Finero Mafic Complex
1001 (Ivrea-Verbano Zone). Journal of Petrology 55, 1239-1240.
1002 Zanetti, A., Giovanardi, T., Langone, A., Tiepolo, M., Wu, F.-Y., Dallai, L., Mazzucchelli, M.,
1003 2016. Origin and age of zircon-bearing chromitite layers from the Finero phlogopite peridotite
1004 (Ivrea–Verbano Zone, Western Alps) and geodynamic consequences. Lithos 262, 58-74.

1005

1006

1007

1008

1009

1010

1011

1012

1013

1014

1015

1016

1017

1018

1019

1020 **Figure captions**

1021

1022 Figure 1: Geological map of the Finero area, modified after Mazzucchelli et al. (2014).

1023

1024 Figure 2: A) Sample FI09C06 crosscutting the host harzburgite foliation. The centre of the dyke is
1025 formed by the Leucocratic Zone, whereas the melanocratic zones (i.e. the Orthopyroxene Zone,
1026 Early Amphibole Zone, and Late Amphibole Zone) are indistinguishable; B) phlogopite vein
1027 cutting the Orthopyroxene Zone; C–F) occurrences of sapphirine in sample FI09C06 (C and D) and
1028 sample FI9664 (E and F). The figures show the increase of sapphirine size, from μm (C) to mm (D
1029 and E) and cm scale (F).

1030

1031 Figure 3: Primitive mantle (PM)-normalised bulk rock trace elemental patterns of a gabbroic dyke
1032 and host harzburgite. PM values are from McDonough and Sun (1995). Literature values from the
1033 harzburgite-pyroxenite association of (1) Hartmann and Wedephol (1993) and nepheline-bearing
1034 hornblende syenitic dykes of (2) Stähle et al. (2001) are reported for comparison.

1035

1036 Figure 4: Orthopyroxene major elemental contents from host harzburgites, dykes, and literature
1037 data. Plotted literature data are the harzburgite-pyroxenite association orthopyroxene from (1)
1038 Zanetti et al. (1999) and orthopyroxene from sapphirine-bearing rock from the Mafic Complex from
1039 (2) Sills et al. (1983).

1040

1041 Figure 5: Phlogopite major elemental contents from host harzburgites, dykes, and literature data.
1042 Plotted literature data are: harzburgite-pyroxenite association phlogopite from (1) Zanetti et al.
1043 (1999).

1044

1045 Figure 6: Amphibole major elemental contents from host harzburgites, dykes, and literature data.
1046 Plotted literature data are: harzburgite-pyroxenite association amphibole compositions from (1)
1047 Zanetti et al. (1999) and (2) Morishita et al. (2008), amphibole from apatite-rich veins in the FPP

1048 from (1) Zanetti et al. (1999) and (2) Morishita et al. (2008), and amphibole from sapphirine-
1049 bearing rock from the Mafic Complex from (3) Sills et al. (1983).

1050

1051 Figure 7: Sapphirine compositions plotted in the (MgO + FeO)–(Cr₂O₃ + Fe₂O₃ + Al₂O₃)–SiO₂
1052 diagram (mol. %). Literature data are from sapphirine of the Finero Mafic Complex (Sills et al.,
1053 1983) and sapphirine 1 of Higgins et al. (1979).

1054

1055 Figure 8: REE patterns of clinopyroxene and amphibole from the gabbroic dykes and the respective
1056 host rocks divided for samples and position. Values are normalised to Chondrite-I (CI, values from
1057 Lyubetskaya and Korenaga (2007); $\delta^{18}\text{O}$ values (normalised to SMOW) from phases of sample
1058 FI09C06 are reported near the REE patterns according to their positions in the sample.

1059

1060 Figure 9: PM-normalised trace elemental patterns of clinopyroxene from host harzburgite. PM
1061 values are from McDonough and Sun (1995). Plotted literature data are: clinopyroxene and
1062 amphibole average compositions from the harzburgite-pyroxenite association from (1) Zanetti et al.
1063 (1999) and (2) Morishita et al. (2008), clinopyroxene and amphibole average from apatite-rich veins
1064 in the FPP from (1) Zanetti et al. (1999) and (2) Morishita et al. (2008), reported as apatite veins.

1065

1066 Figure 10: PM-normalised trace elemental patterns of amphiboles from gabbroic dyke and host
1067 harzburgite. PM values are from McDonough and Sun (1995).

1068

1069 Figure 11: $\delta^{18}\text{O}$ normalised to SMOW. Values from literature are the field of mantle and variation
1070 of MORB from Rollinson (1993), and mantle ultramafics and mantle-derived melts (*) from
1071 Bindeman (2008). Finero literature data are reported from the harzburgite-pyroxenite association of
1072 Hartmann and Wedephol (1993) and Selverstone and Sharp (2011) and from chromitite in dunite
1073 bodies from Zanetti et al. (2016).

1074

1075 Figure 12: $^{143}\text{Nd}/^{144}\text{Nd}$ vs $^{87}\text{Sr}/^{86}\text{Sr}$ recalculated at 225 Ma for amphibole and plagioclase from the
1076 various zones of sample FI09C06 (host and dyke): (1) amphibole data of the FPP from Obermiller
1077 (1994); (2) bulk rock data of the Finero Mafic Complex from Lu et al. (1997b); (3) data from an
1078 alkaline dyke in the FPP from Stähle et al. (1990); (4) data from an alkaline dyke in the FPP from
1079 Stähle et al. (2001); (5) amphibole and apatite data from discordant apatite-bearing veins in the FPP
1080 from Morishita et al. (2008); (6) Mesozoic shoshonitic magmatism (SS: silica saturated; US:
1081 undersaturated in silica) in the Predazzo area from Casetta et al. (2018a, b); Depleted MORB
1082 Mantel (DMM) from Workman and Hart (2005). The mixing model was calculated between the two
1083 end-members: the alkaline dyke S9 of Stähle et al. (1990) and the hosting peridotite FI09C06. Data
1084 for the melt in equilibrium with the alkaline dyke S9 are: $^{143}\text{Nd}/^{144}\text{Nd} = 0.512607$, $^{87}\text{Sr}/^{86}\text{Sr} =$
1085 0.703720 (from Stähle et al., 1990; recalculated at 225 Ma), Nd = 8.333 ppm, and Sr = 830 ppm
1086 (calculated from LA-ICP-MS plagioclase analysis of albitite dykes similar to the dyke of Stähle et
1087 al., 1990, using the K_d of Dohmen and Blundy, 2014; average Nd = 0.25 ppm, Sr = 5810 ppm).
1088 Data for the melt in equilibrium with the host FPP peridotite are $^{143}\text{Nd}/^{144}\text{Nd} = 0.512130$, $^{87}\text{Sr}/^{86}\text{Sr} =$
1089 0.708501 (recalculated at 225 Ma), Nd = 67.5 ppm, and Sr = 909 ppm (calculated using the K_d of
1090 Ionov et al., 2002).

Figure 1

[Click here to download high resolution image](#)

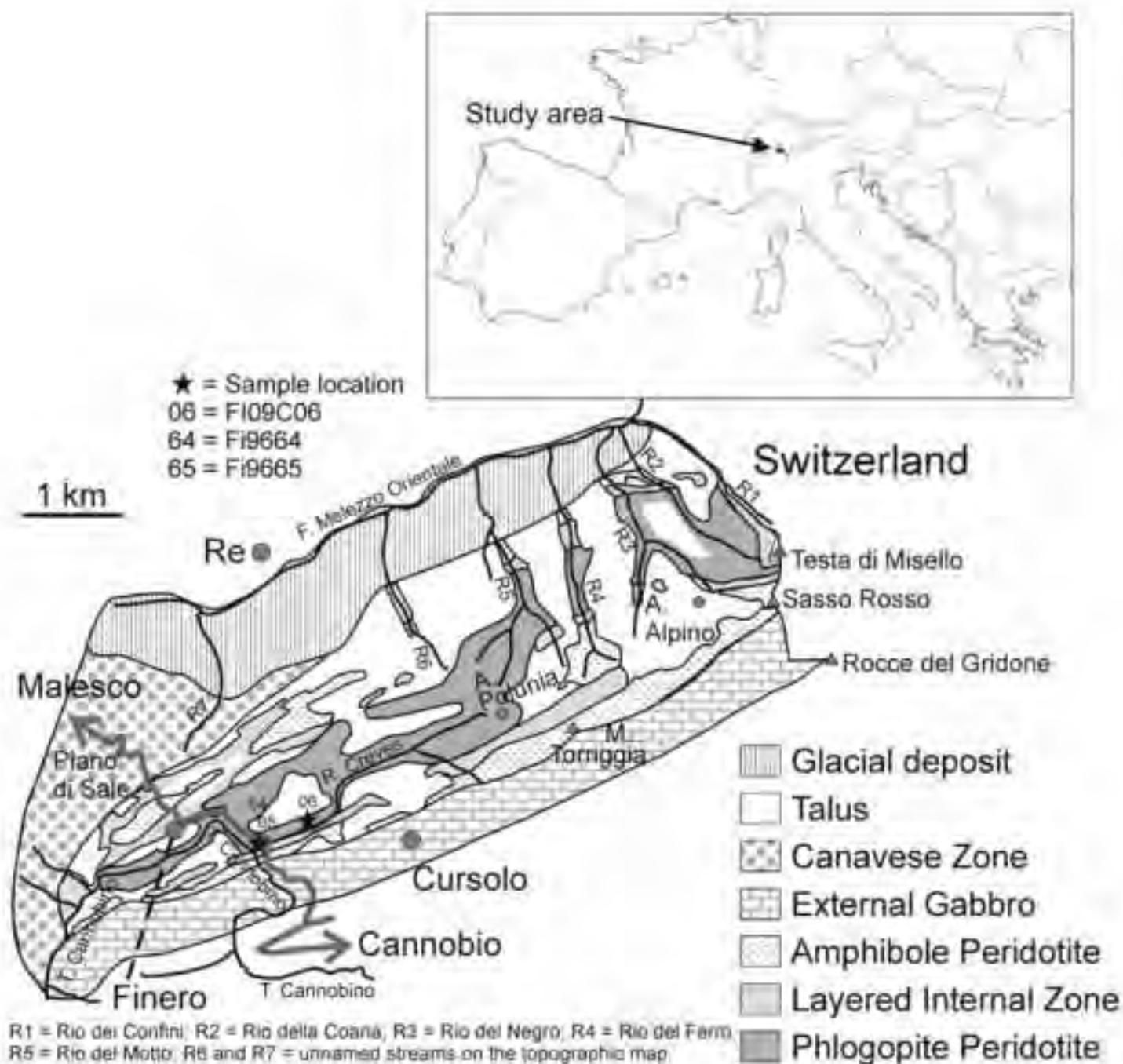


Figure 2
[Click here to download high resolution image](#)

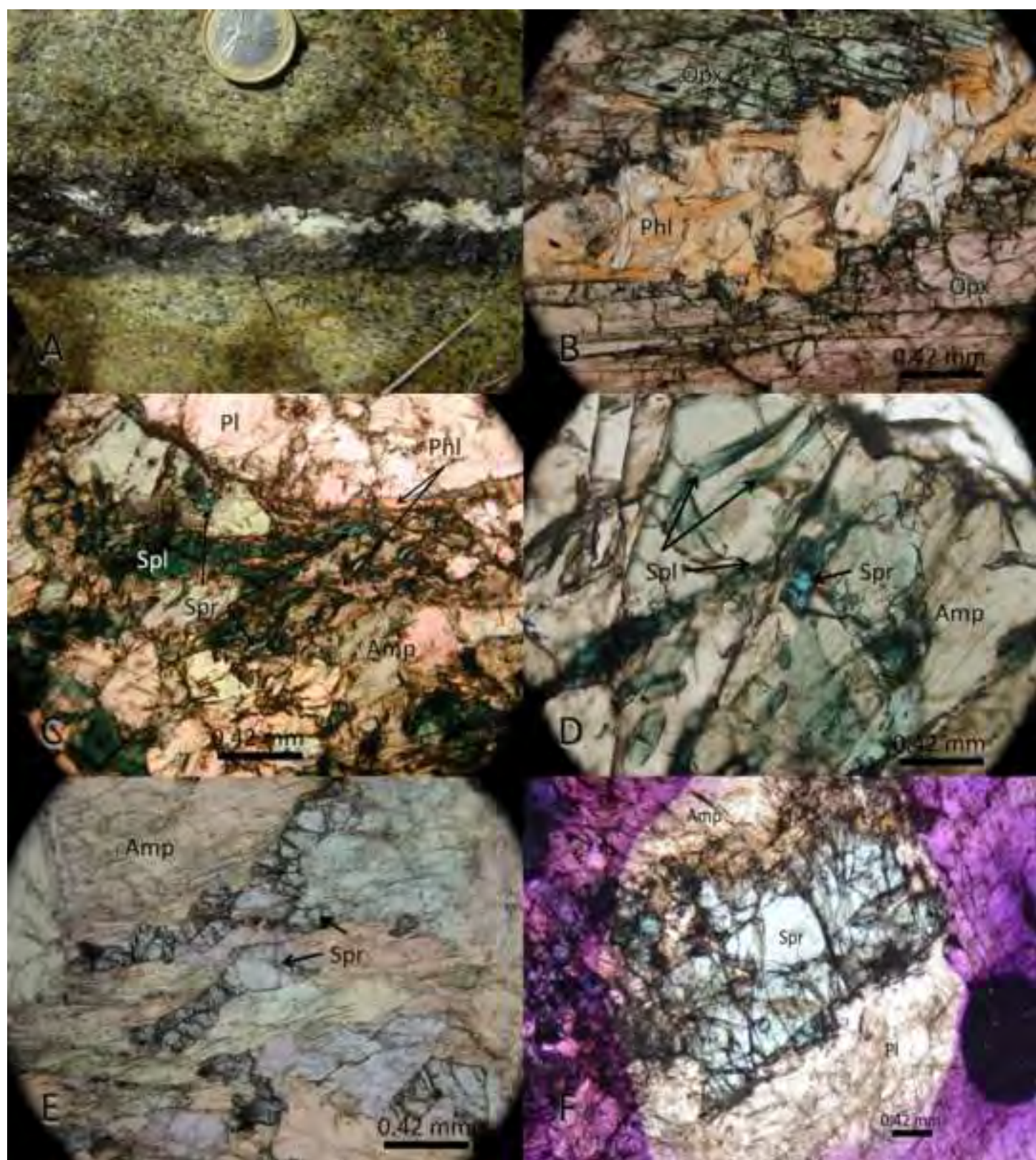


Figure 3
[Click here to download high resolution image](#)

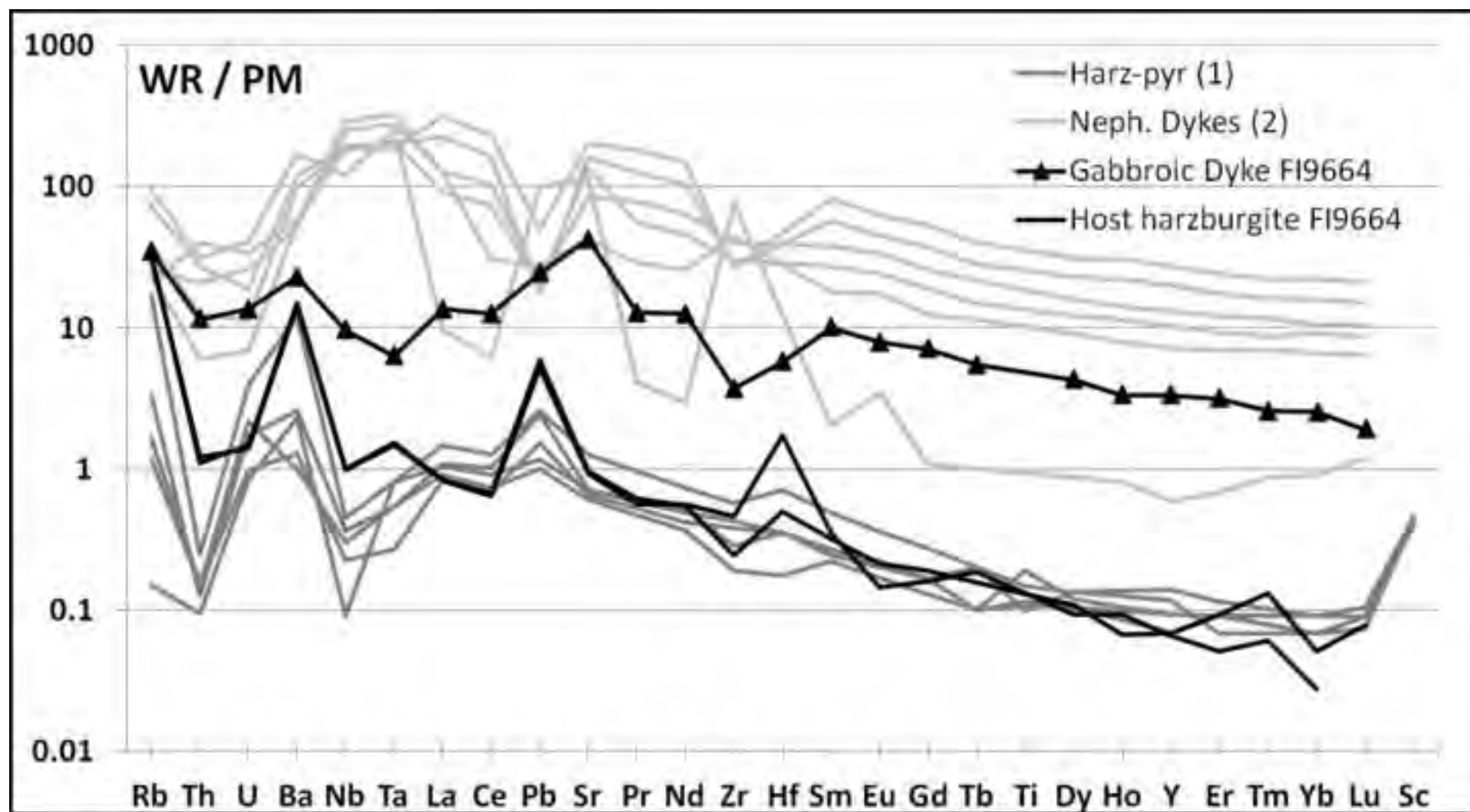


Figure 4

[Click here to download high resolution image](#)

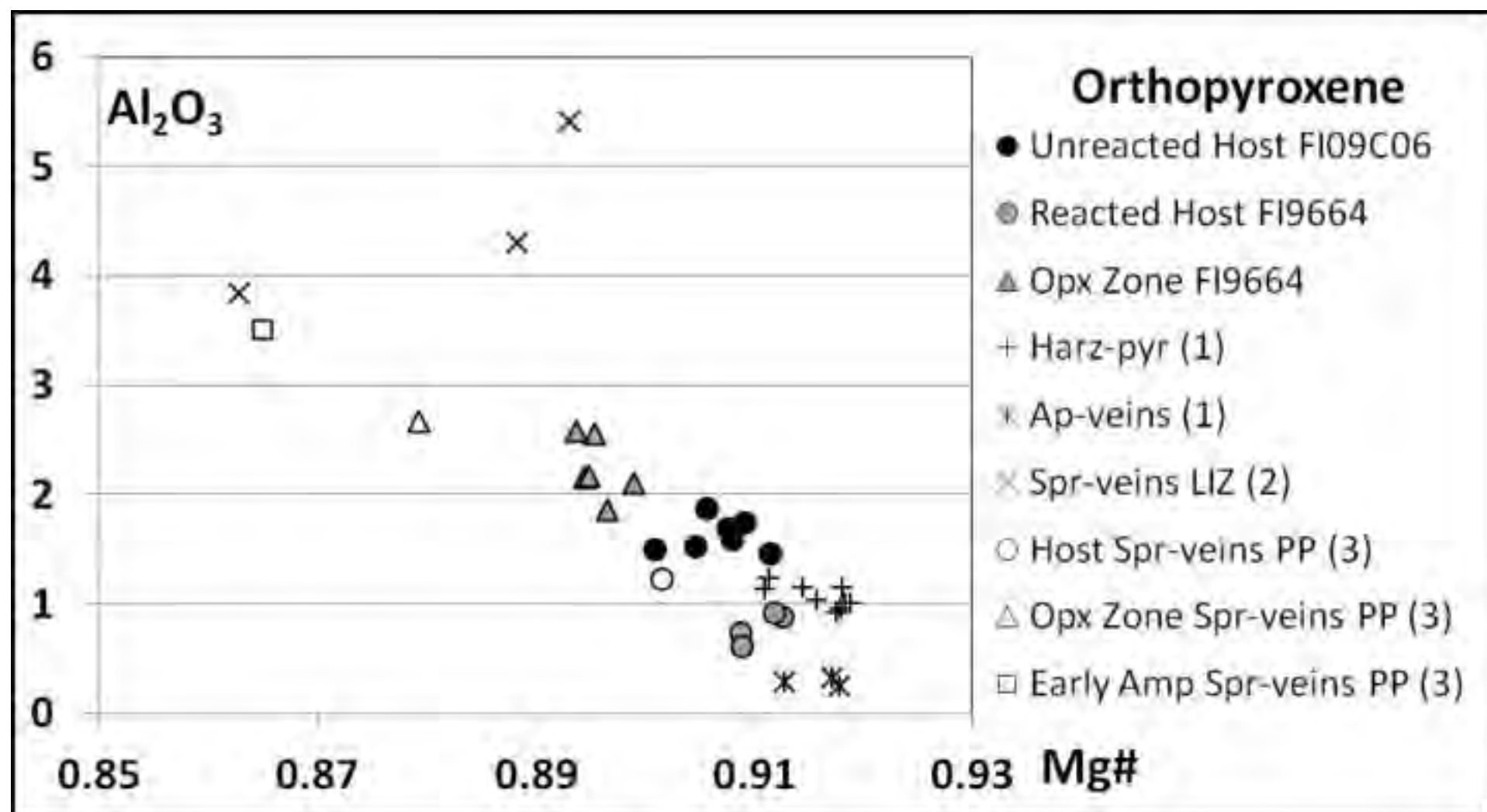


Figure 5

[Click here to download high resolution image](#)

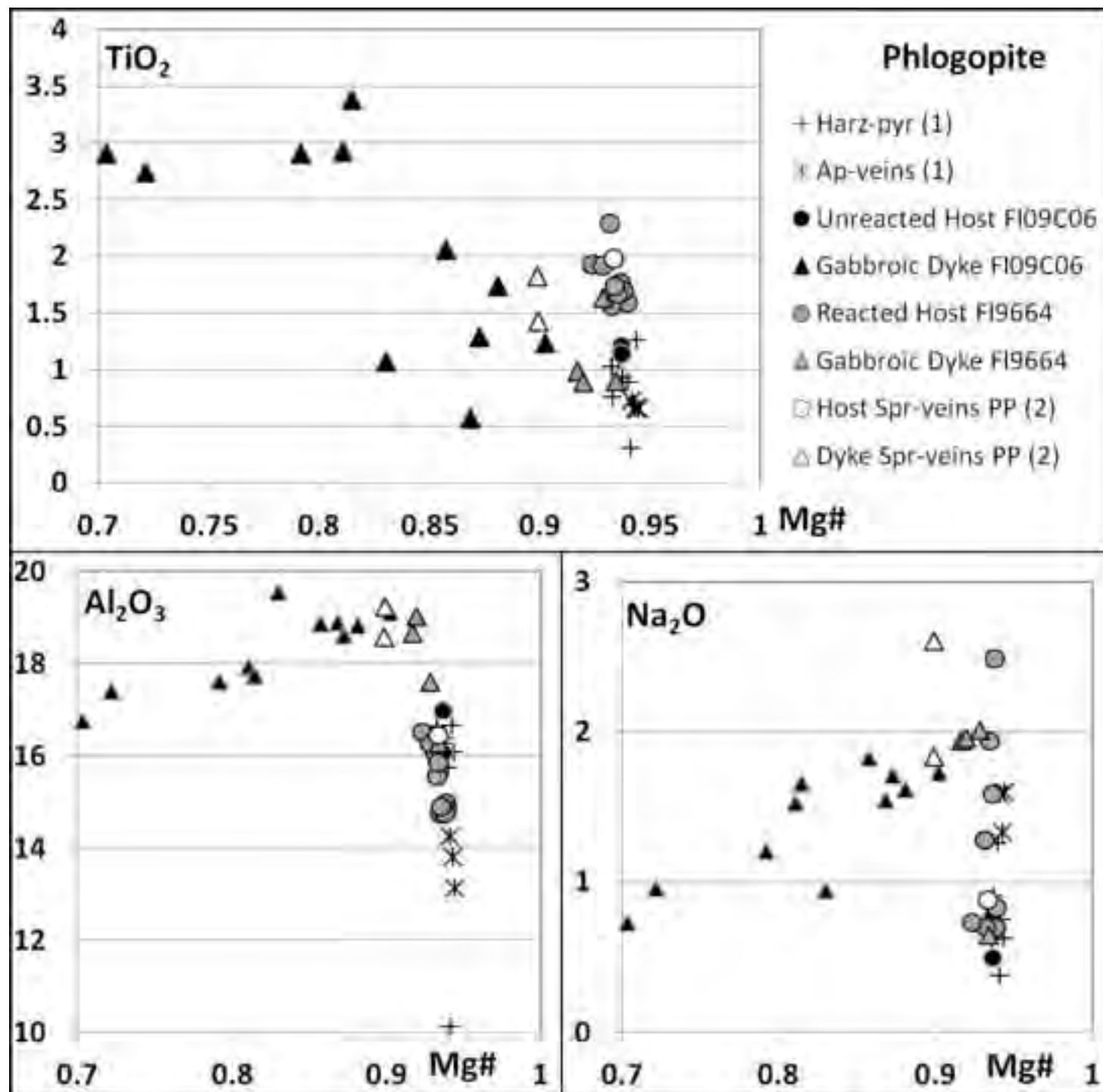


Figure 6

[Click here to download high resolution image](#)

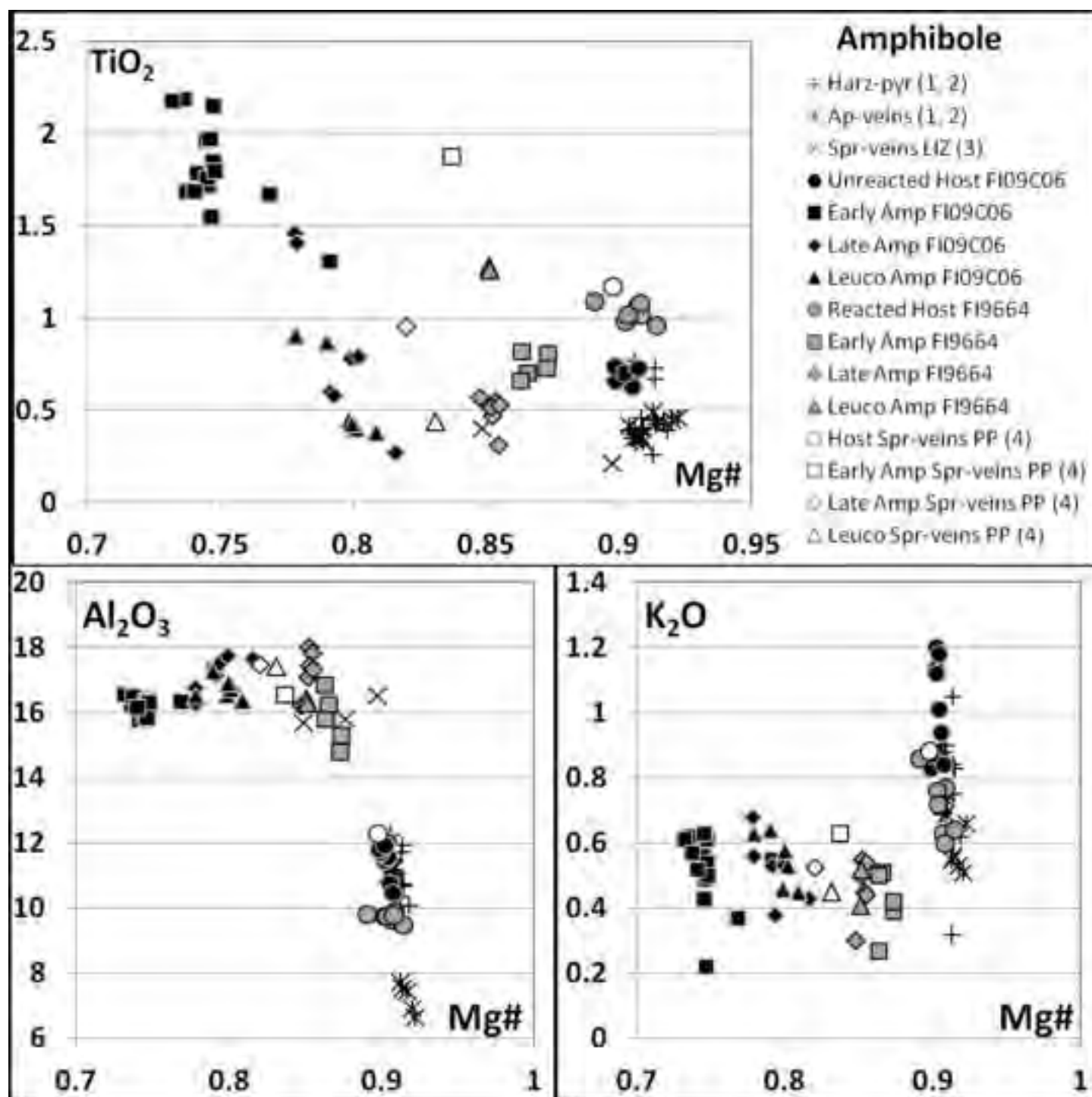


Figure 7
[Click here to download high resolution image](#)

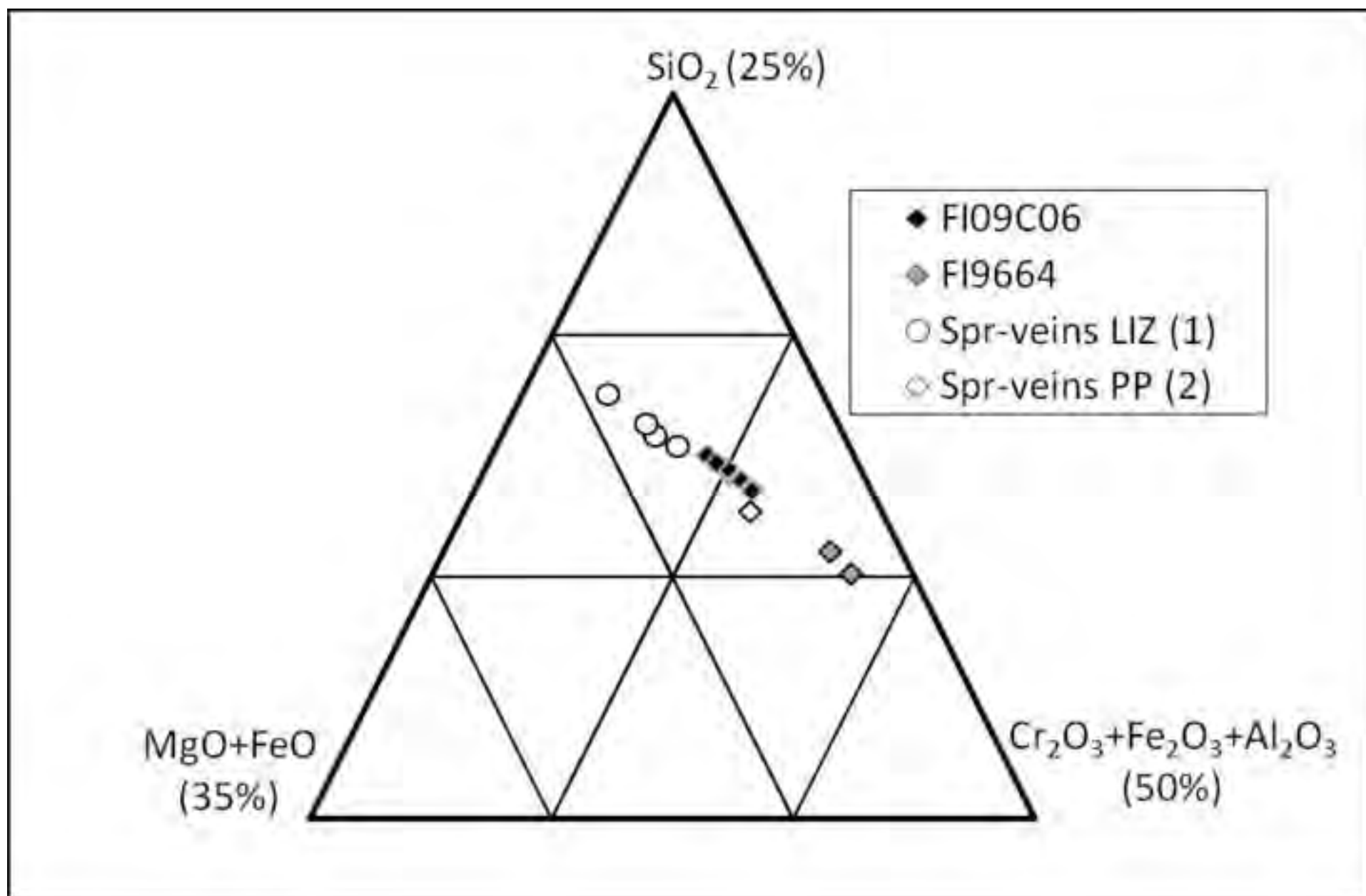


Figure 8
[Click here to download high resolution image](#)

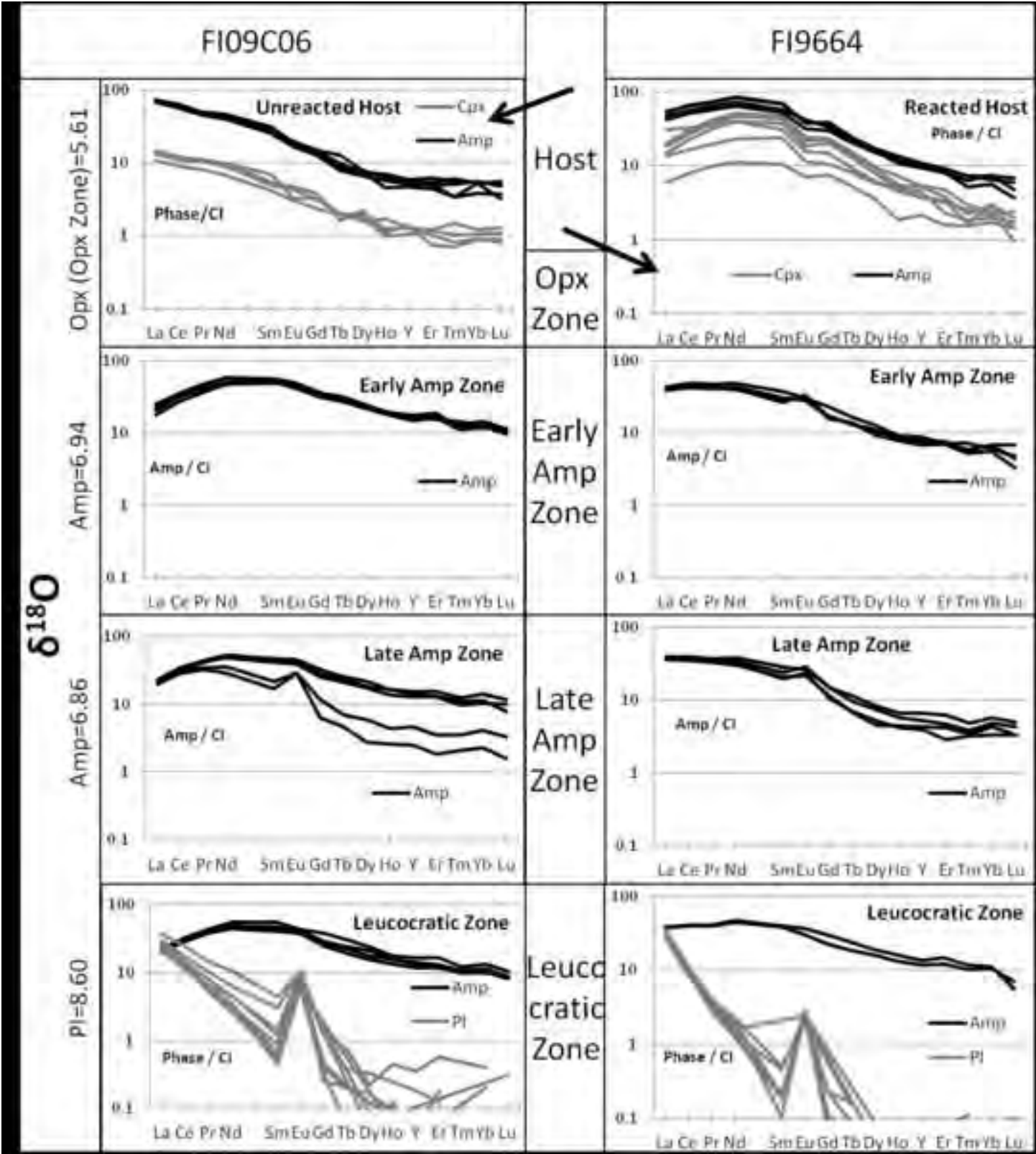


Figure 9
[Click here to download high resolution image](#)

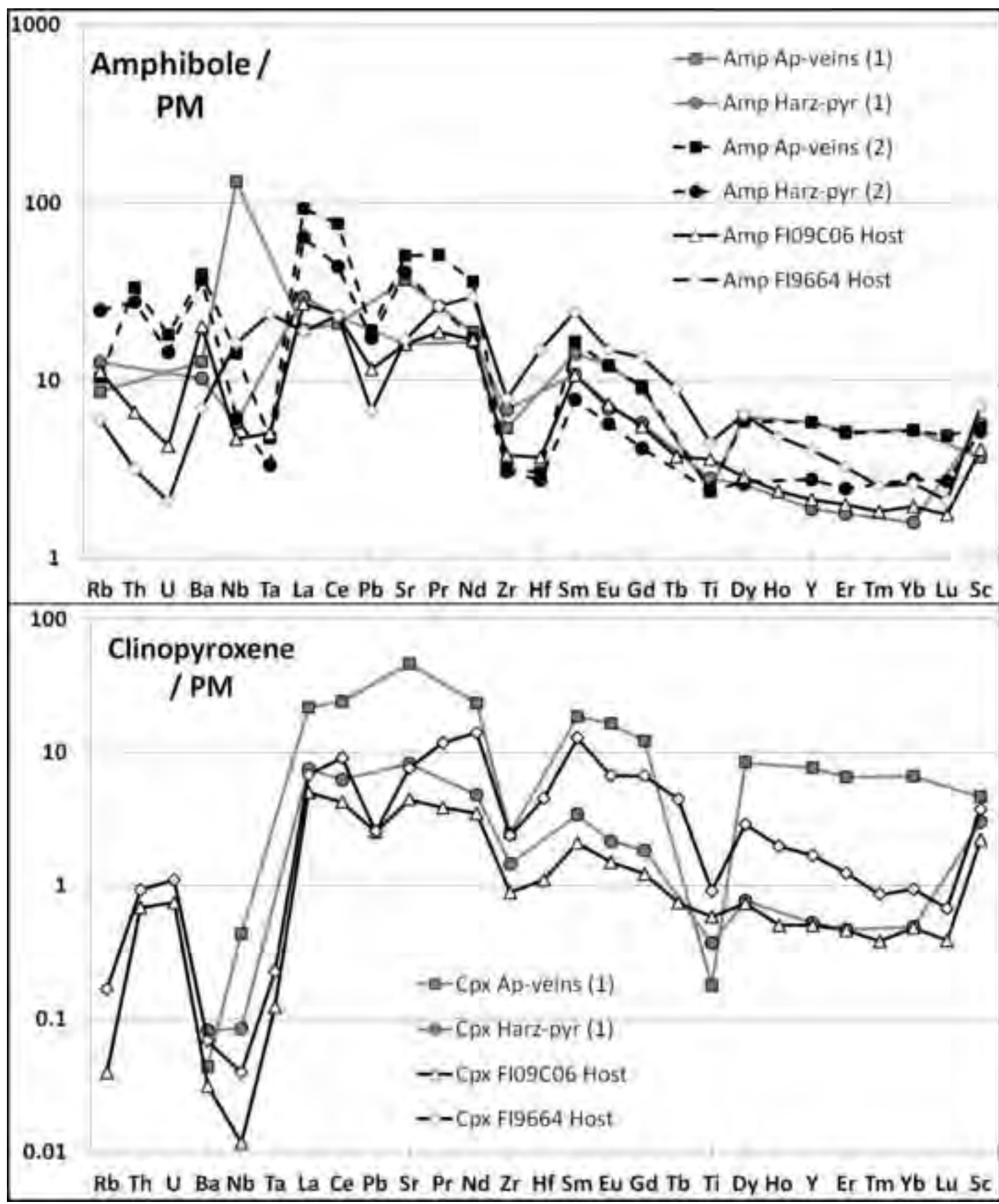


Figure 10
[Click here to download high resolution image](#)

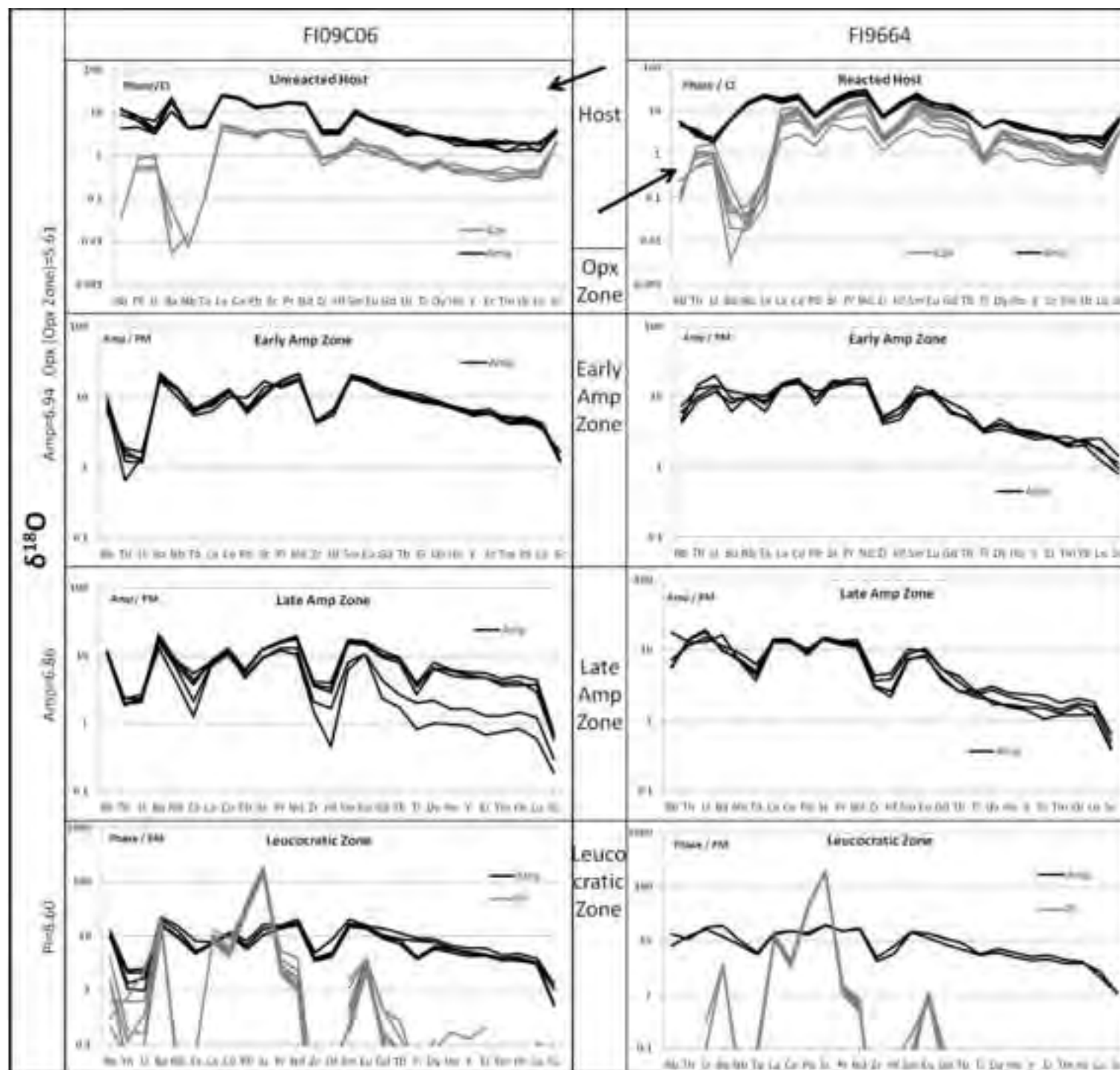


Figure 11

[Click here to download high resolution image](#)

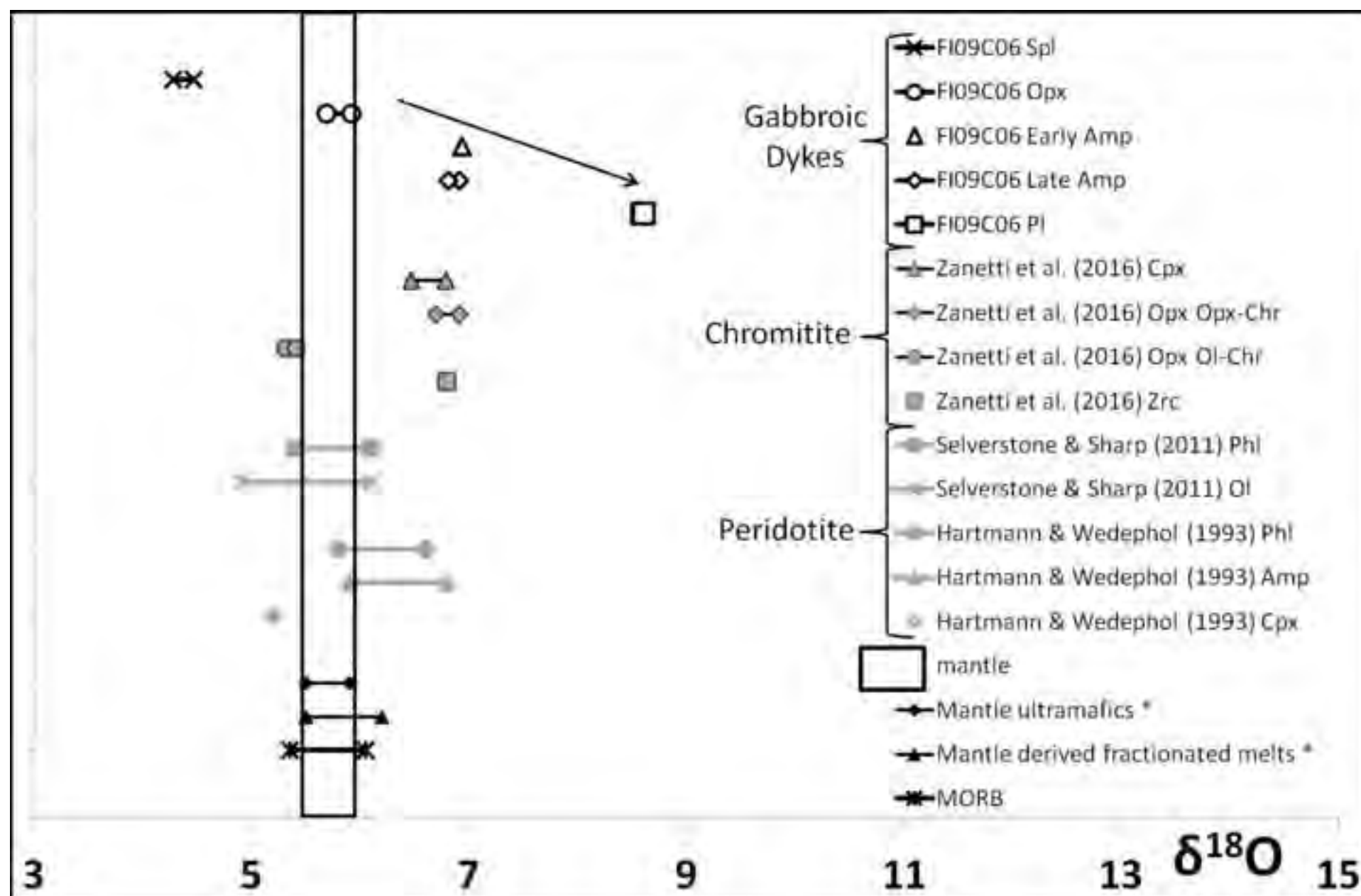


Figure 12

[Click here to download high resolution image](#)

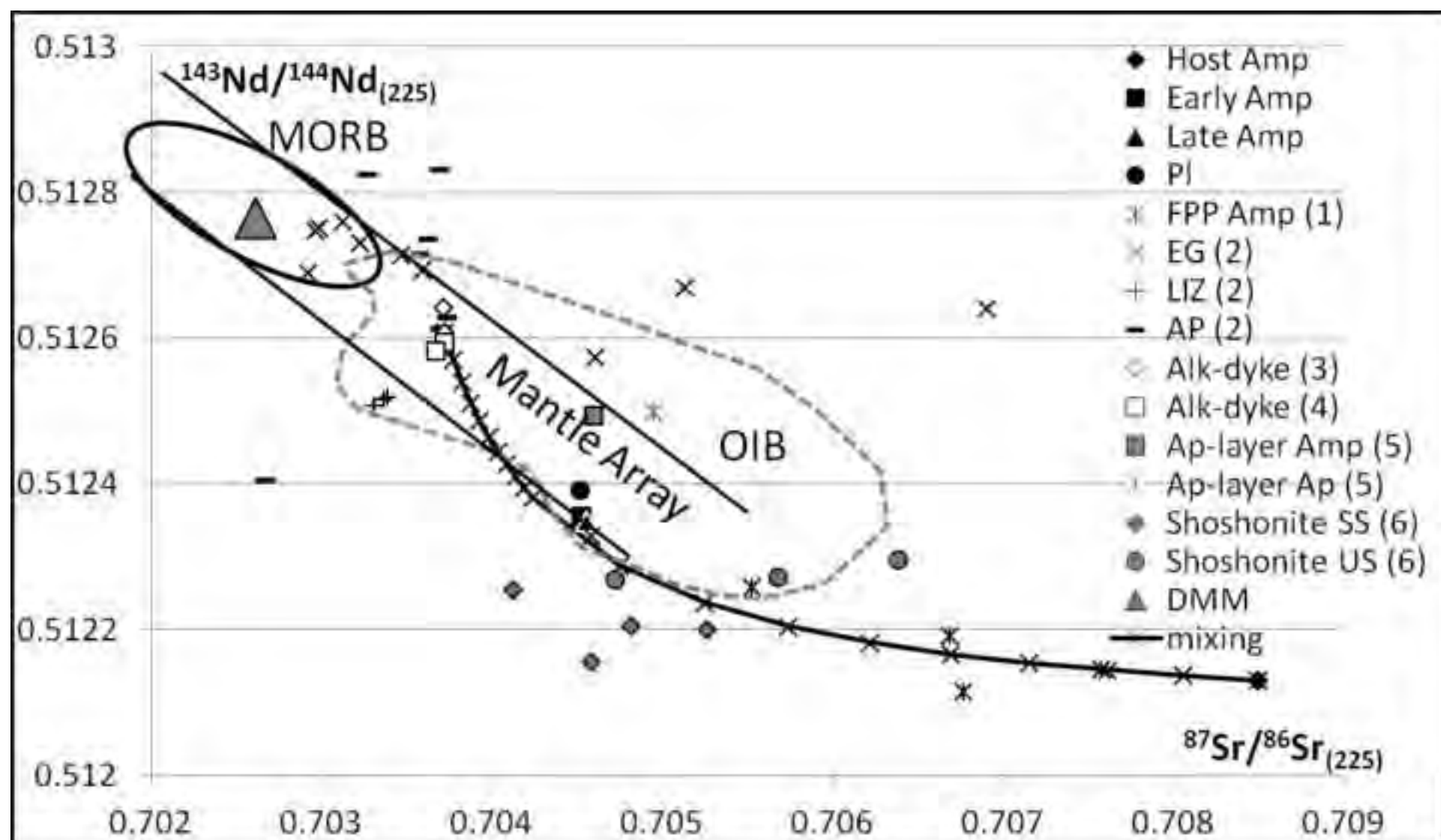


Table 1: O isotopic composition of minerals from the Spr-bearing gabbroic dykes.

Sample	Phase	$\delta^{18}\text{O}$	std. dev.
FI09C06	Early Amp	6.94	0.00
FI09C06	Late Amp	6.86	0.05
FI09C06	Pl	8.60	0.01
FI09C06	Opx	5.81	0.11

Table 2: Sr and Nd isotopic composition of minerals from sample FI09C06 from the Spr-bearing gabbroic dykes and the host peridotite.

Rock	Phase	Rb	Sr	⁸⁷ Sr/ ⁸⁶ Sr	2SE	⁸⁷ Rb/ ⁸⁶ Sr	Nd	Sm	¹⁴³ Nd/ ¹⁴⁴ Nd	2SE	¹⁴⁷ Sm/ ¹⁴⁴ Nd
Host	Amp	6.5	281.2	0.708713	0.000008	0.066372	19.7	4.2	0.512317	0.000008	0.126796
Dyke	Early Amp	6.8	324.4	0.704722	0.000008	0.060834	24.8	8.1	0.512646	0.000008	0.197559
Dyke	Late Amp	8.6	189.5	0.704971	0.000008	0.131167	16.8	4.0	0.512559	0.000006	0.142593
Dyke	Pl	0.6	3109.7	0.704519	0.000008	0.000568	2.2	0.2	0.512482	0.000006	0.061238